Draft version November 29, 2012
Preprint typeset using LaTeX style emulateapj v. 5/2/11

arXiv:1211.6492v1 [astro-ph.GA] 28 Nov 2012

THE GALACTIC CENSUS OF HIGH- AND MEDIUM-MASS PROTOSTARS. II. LUMINOSITIES AND EVOLUTIONARY STATES OF A COMPLETE SAMPLE OF DENSE GAS CLUMPS

Bo Ma(馬波)[1], Jonathan C. Tan[1,2], Peter J. Barnes[1]
Department of Astronomy, University of Florida, FL, 32611, USA and
Department of Physics, University of Florida, FL, 32611, USA

Draft version November 29, 2012

ABSTRACT

The Census of High- and Medium-mass Protostars (CHaMP) is the first large-scale ($280^\circ < l < 300^\circ$, $-4^\circ < b < 2^\circ$), unbiased, survey of massive molecular clumps in the Milky Way at parsec-scale resolution using 90 and 110 GHz line emission. Barnes et al. (2011, hereafter Paper I) presented the source catalog of ~300 dense molecular clumps from their Mopra (ATNF) HCO$^+$(1-0) maps. Here we use archival Spitzer, MSX, IRAS and mm continuum data to construct the spectral energy distributions (SEDs) of these clumps. We fit two temperature grey-body models to the SEDs and use these to derive bolometric fluxes and, given the adopted clump distances, bolometric luminosities, L. We also consider the temperatures, T_c, of the colder component of the model fit as an approximate measure of the mean dust temperature in the clump. We evaluate the ratio, L/M, where M is the mass derived from HCO$^+$(1-0) emission. We find the clumps have $10L_\odot \lesssim L \lesssim 10^{6.5}L_\odot$ and $0.1 \lesssim L/M/[L_\odot/M_\odot] \lesssim 10^3$. These values are consistent with theoretical expectations of a clump population that spans a range of instantaneous star formation efficiencies from 0 to $\sim 50\%$. We thus expect L/M to be a good (i.e. strongly varying) evolutionary indicator of the star cluster formation process. We find significant correlations of the ratio of warm to cold component flux and of the cold component temperature with L/M. We also find a near linear relation between *Spitzer*-IRAC specific intensity and L/M, and so we propose its use as an empirical star formation efficiency indicator. The lower bound of the distribution of L/M of the clumps suggests the star formation efficiency per free-fall time is $\epsilon_{\rm ff} < 0.2$. We do not find strong correlations of L/M with mass surface density, velocity dispersion or virial parameter. Similar to previous studies, we find a linear relation between L and dense gas mass as measured by HCO$^+$(1-0) line luminosity, $L_{\rm HCO^+(1-0)}$, although there is a large scatter for any given individual clump. The sensitive nature of the CHaMP survey allows us to explore this relation down to much lower luminosity sources, $\sim 30\ L_\odot$, than has been done before. Fitting together with extragalactic systems, the linear relation still holds, extending over about 10 orders of magnitude in luminosity. The complete nature of the CHaMP survey over a several kiloparsec extent in the Milky Way also allows us to derive an intermediate measurement that bridges the scales of individual clumps and whole galaxies.

Subject headings: stars: formation — stars: pre–main-sequence — ISM: dust — surveys

1. INTRODUCTION

Stars form from the gravitational collapse of the densest regions of giant molecular clouds (GMCs). In particular star clusters, likely the dominant mode of star formation (Lada & Lada 2003; Gutermuth et al. 2009), are born from ~ parsec-scale gas *clumps* within GMCs. However, many open questions remain (see, e.g. McKee & Ostriker 2007; Tan et al. 2012; Hennebelle & Falgarone 2012). How are GMCs formed out of the diffuse interstellar medium? Why does star formation occur in only a small fraction of the available gas in GMCs? What is the star formation rate and efficiency over the GMC lifetime and what processes control this? What is the timescale of star cluster formation: is it fast (Elmegreen 2000, 2007) or slow (Tan et al. 2006) with respect to the free-fall time? What processes control the evolution and overall star formation efficiency of a star-forming clump?

To help address some of these open questions, Barnes et al. (2011, hereafter Paper I) have designed a multi-wavelength survey, the Census of High- and Medium-mass Protostars (CHaMP). Starting in the 3mm-wave band, the aim of CHaMP has been to map a complete sample of molecular gas structures in a $20^\circ \times 6^\circ$ region in the southern Galactic plane ($280^\circ < l < 300^\circ$, $-4^\circ < b < +2^\circ$). Using the 4m Nanten telescope, this region was first surveyed in the J=1-0 transitions of ^{12}CO, ^{13}CO, C^{18}O and HCO$^+$ (Yonekura et al. 2005; Paper I). This sequence of species traces progressively higher densities and the mapping was carried out in this order so as to identify all the locations of dense gas, without having to map the entire region in the tracers of the densest gas. So ^{13}CO was only observed where the ^{12}CO integrated intensity was above 10 K km s^{-1}, and C^{18}O and HCO$^+$ were observed where ^{13}CO was brighter than 5 K km s^{-1}. Then a follow-up campaign was begun to map the dense gas regions found in the Nanten survey. The follow-up is conducted in a number of 3mm molecular transitions with the 22m Mopra telescope at much higher sensitivity and angular resolution than Nanten telescope (Paper I). This observing strategy distinguishes the CHaMP survey from all other Galactic plane surveys of dense gas, such as MALT90 (Foster et al. 2011).

In Paper I, maps of the CHaMP regions in HCO$^+$(1-0) line emission observed by the Mopra telescope were presented.

A total of 303 massive molecular clumps were identified. This sample has the following properties: integrated line intensities 1-30 K km s^{-1}, linewidths 1-9 km s^{-1}, FWHM sizes 0.2-2 pc, mean mass surface densities $\Sigma \sim 0.01$ to ~ 1 g cm^{-2} and masses ~ 10 to $\sim 10^4\,M_\odot$.

In this paper we use archival infrared and millimeter data to investigate the SEDs and luminosities of these HCO^+ clumps, with the goal being to characterize their evolutionary state with respect to star cluster formation. The paper is organized as follows. §2 describes the IR and mm data used in this study. §3 describes our methods of estimating clump fluxes. §4 presents our results, including the clump masses, bolometric fluxes, bolometric luminosities, luminosity-to-mass ratios, warm and hot component fluxes, and cold component temperatures and bolometric temperatures. In particular we emphasize the potential use of the luminosity-to-mass ratio as an evolutionary indicator for star cluster formation. §5 presents further discussion, including searches for potential correlation of luminosity-to-mass ratio with clump mass surface density and virial parameter. It also discusses the luminosity versus HCO^+ line luminosity relation from clumps to whole galaxies. §6 summarizes our conclusions.

2. INFRARED AND MILLIMETER OBSERVATIONAL DATA

The first goal of this paper is to measure fluxes at various wavelengths coming from the CHaMP clumps. Here we describe the main observational datasets that we use to derive these fluxes.

2.1. *MSX*

The Midcourse Space Experiment (MSX) was launched in April 1996. It conducted a Galactic plane survey ($0° < l < 360°$, $|b| < 5°$), which covers all the CHaMP clumps. The four MSX band wavelengths are centered at 8.28, 12.13, 14.65 and 21.3 μm. The best image resolution is $\sim 18''$ in the 8.28 μm band, with positional accuracy of about $2''$. The instrumentation and survey are described by Egan & Price (1996). Calibrated images of the Galactic plane were obtained from the online MSX image server at the IPAC website at: http://irsa.ipac.caltech.edu/data/MSX/. We assume the absolute fluxes of the MSX data are accurate to about 20%.

2.2. *IRAS*

The Infrared Astronomical Satellite (IRAS) performed an all sky survey at 12, 25, 60 and 100 μm. The nominal resolution is about $4'$ at 60μm. HIRES uses the Maximum Correlation Method (MCM, Aumann et al. 1990) to produce higher resolution images, better than $1'$ at 60 μm. Sources chosen for processing with HIRES were processed at all four IRAS bands with 20 iterations. The pixel size was set to $15''$ with a 1° field centered on the target. The absolute fluxes of the IRAS data are expected to be accurate to about 20%.

2.3. *Spitzer IRAC*

The Spitzer InfraRed Array Camera (IRAC) is a four-channel camera that provides simultaneous $5.2' \times 5.2'$ images at 3.6, 4.5, 5.8, and 8 μm with a pixel size of $1.2'' \times 1.2''$ and angular resolution of about $2''$ at 8 μm. We searched the Spitzer archive at http://irsa.ipac.caltech.edu/applications/Spitzer/SHA/ for IRAC data near the positions of our HCO^+ clumps. We found IRAC data for 284 out of our 303 clumps. Most of these data are from two large survey programs: PID 189 (Churchwell, E., "The SIRTF Galactic Plane Survey") and PID 40791 (Majewski, S., "Galactic Structure and Star Formation in Vela-Carina"). We used the post basic calibration data to estimate the fluxes of these clumps, which we assume has a 20% uncertainty.

2.4. *Millimeter data*

Hill et al. (2005) carried out a 1.2-mm continuum emission survey toward 131 star-forming complexes using the Swedish ESO Submillimetre Telescope (SEST) IMaging Bolometer Array (SIMBA). SIMBA is a 37-channel hexagonal bolometer array operating at a central frequency of 250 GHz (1.2mm), with a bandwidth of 50 GHz. It has a half power beam width of $24''$ for a single element, and the separation between elements on the sky is 44 arcsec. They have provided the 1.2-mm flux for 404 sources, 15 of which are in our sample.

3. DATA ANALYSIS

3.1. *Definition of Clump Angular Area*

Paper I mapped the CHaMP region in HCO^+(1-0) line emission using the 22m Mopra telescope, identifying 303 massive molecular clumps. Barnes et al. defined elliptical sizes based on 2D Gaussian fitting for each HCO^+ clump. The ellipse size quoted in columns 9 and 10 of Table 4 of Paper I is the FWHM angular size of the major and minor axes of the Gaussian fit. Barnes et al. evaluated clump masses, M, based on integrating the derived column density distribution over the full area of the Gaussian profile ($M_{\rm col}$ listed in column 9 of their Table 5). Note the derivation of mass surface densities and masses from the observed HCO^+(1-0) intensity depends on: (1) the assumed excitation temperature ($T_{\rm ex} = 10$ K was adopted as a fiducial value in Paper I; a value of 30 K would raise masses by a factor of about 40%; note, that corrections for optical depth were made given the adopted value of $T_{\rm ex}$); (2) the abundance of HCO^+ ($X_{\rm HCO^+} \equiv n_{\rm HCO^+}/n_{\rm H2} = 1.0 \times 10^{-9}$ was adopted in Paper I; systematic uncertainties of a factor of ~ 3 may be expected, although relative clump masses should be more accurate); and (3) the distance to the sources (a combination of literature values based on association with nearby objects and kinematic estimates were used; distance uncertainties of about 30% are expected, i.e. leading to $\sim 60\%$ uncertainties in M).

To measure the continuum fluxes at various wavelengths coming from the CHaMP HCO$^+$ clumps, we define the clump size as two times larger than the FWHM ellipse derived in Paper I, i.e. its radial extent is equal to 1 FWHM at a given position angle. For a 2D Gaussian, the area inside this ellipse encloses 93.75% of the total flux. Thus with this definition of clump size we expect to enclose close to 100% of M_{HCO^+} measured in Paper I.

The clumps are highly clustered in space so that on a scale of two times the FWHM ellipse the majority of them, $\sim 70\%$ of the sample, suffer from overlap with a neighboring clump ($\sim 30\%$ overlap on the scale of one times the FWHM ellipse). While the original clump definition from Paper I also used their velocity space information, often nearby clumps also overlap in velocity. We have developed an approximate method to estimate the fluxes of these clumps where there are image pixels belonging to more than one ellipse. We first calculate the angular distance, normalized by the size of the ellipse, from the overlapped pixel to the center of each clump. This normalized angular distance is defined as $r_{\mathrm{norm}} = ((d_x/a)^2 + (d_y/b)^2)^{1/2}$, where d_x and d_y are the angular distance from the overlapped pixel to the minor and major axis of each ellipse, and a and b are the angular sizes of the major and minor axis of the ellipse. Then the flux of each overlapped pixel is assigned to its nearest ellipse according to this normalized angular distance.

3.2. *Clump and Background Flux Measurements*

The MSX and IRAS data exist for all 303 CHaMP clumps and these form the basis for our spectral energy distribution measurements. We describe here the method we use to derive the fluxes from the clumps based on these imaging data. We then describe how we utilize the mid-infrared IRAC data and the mm data where it is available.

Using the coordinates, sizes and geometries of the HCO$^+$ sources, fluxes were deduced first by directly integrating over the images, this total flux being expressed as $F_{\nu,\mathrm{tot}}$. However, we expect that some fraction of this flux can come from foreground and background sources along the line of sight that are not associated with the clump. For simplicity we refer to this foreground and background emission as the "background flux", $F_{\nu,b}$. We evaluate $F_{\nu,b}$ as the median pixel value in the region between the clump ellipse and an ellipse twice as large (i.e. four times the FWHM size of Paper I), excluding areas that are part of other clumps.

In the end, we derived two fluxes: without and with background subtracted, which are $F_{\nu,\mathrm{tot}}$ and $F_\nu = F_{\nu,\mathrm{tot}} - F_{\nu,b}$, respectively. The error of the fluxes are estimated from the combination of two terms. The first is the uncertainty in the absolute flux from the particular telescope. The data used here are generally assumed to be accurate to about 20%. The second term is from the background subtraction. Since in the Galactic plane it is often difficult to estimate the background emission, we treat the background level as the error term in our flux error estimation. So the fractional error is $(0.2^2 + (\mathrm{F}_{\nu,\mathrm{b}}/\mathrm{F}_{\nu,\mathrm{tot}})^2)^{1/2}$. In the following, we have carried out the analysis for both flux estimates, $F_{\nu,\mathrm{tot}}$ and F_ν.

Next we use a two temperature grey body model to fit the spectral energy distribution (SED) in order to estimate the bolometric fluxes, F_{tot} (no background subtracted) and F (background subtracted), (calculated by integrating over the fitted SED and assuming negligible flux escapes in the near-IR and shorter wavelengths) and temperatures of the clumps, following the method of Hunter et al. (2000) and Faúndez et al. (2004). Each temperature component of the grey body model is described by:

$$F_\nu = \Omega B_\nu(T)\{1 - \exp(-\tau_\nu)\} \tag{1}$$

where $B_\nu(T) = (2h\nu^3/c^2)/[\exp(h\nu/kT) - 1]$ is the Planck function for the black body flux density (where c is the speed of light, h is the Planck constant and k is the Boltzmann constant), Ω is the angular size of the source, and T is the temperature. The dependence of the optical depth, τ_ν, with frequency, ν, is given by:

$$\tau_\nu = \left(\frac{\nu}{\nu_0}\right)^\beta, \tag{2}$$

where β is the emissivity index and ν_0 is the turnover frequency.

In this fitting procedure, for the colder component (subscript "c"), we explored parameter values in the ranges $T_c = 10-50$ K and $\beta_c = 1.0-2.5$. These values of β_c are those expected from laboratory experiments and observational results (see Schnee et al. 2009 and references therein). Also, Faúndez et al. (2004) found β_c to be in this range for their sample of sources. We find ν_0 to generally be in the range $3 - 30$ THz. For the warmer component (subscript "w"), T_w was allowed to have values in the range $100 - 300$ K, while β_w was fixed to 1 following Hunter et al. (2000) and Faúndez et al. (2004). The choice of $\beta_w = 1$ is motivated both by theoretical calculations and by observational evidence (Whittet 1992, pp. 201-203). The angular size of the colder component, Ω_c was set equal to the angular size of the clump, including accounting for reduction due to overlap with other clumps. For the warmer component the angular size, Ω_w, is derived from the best fitting result, always being smaller than the angular size of the clump.

The values of T_c are not particularly well constrained by the IRAS data, which extend to a longest wavelength of only 100 μm. For those 15 sources where we do have mm fluxes reported from SEST-SIMBA, we examine how the two temperature grey body model fit changes when we do make use of the mm flux. Note, for the mm fluxes, not having access to estimates of $F_{\nu,b}$, we assume that background subtraction makes a negligible difference, i.e. $F_{\nu,b} \ll F_\nu$. In Fig. 1 we present the SED and model fits of BYF 73 (G286.2+0.2), which is one of the more massive and actively star-

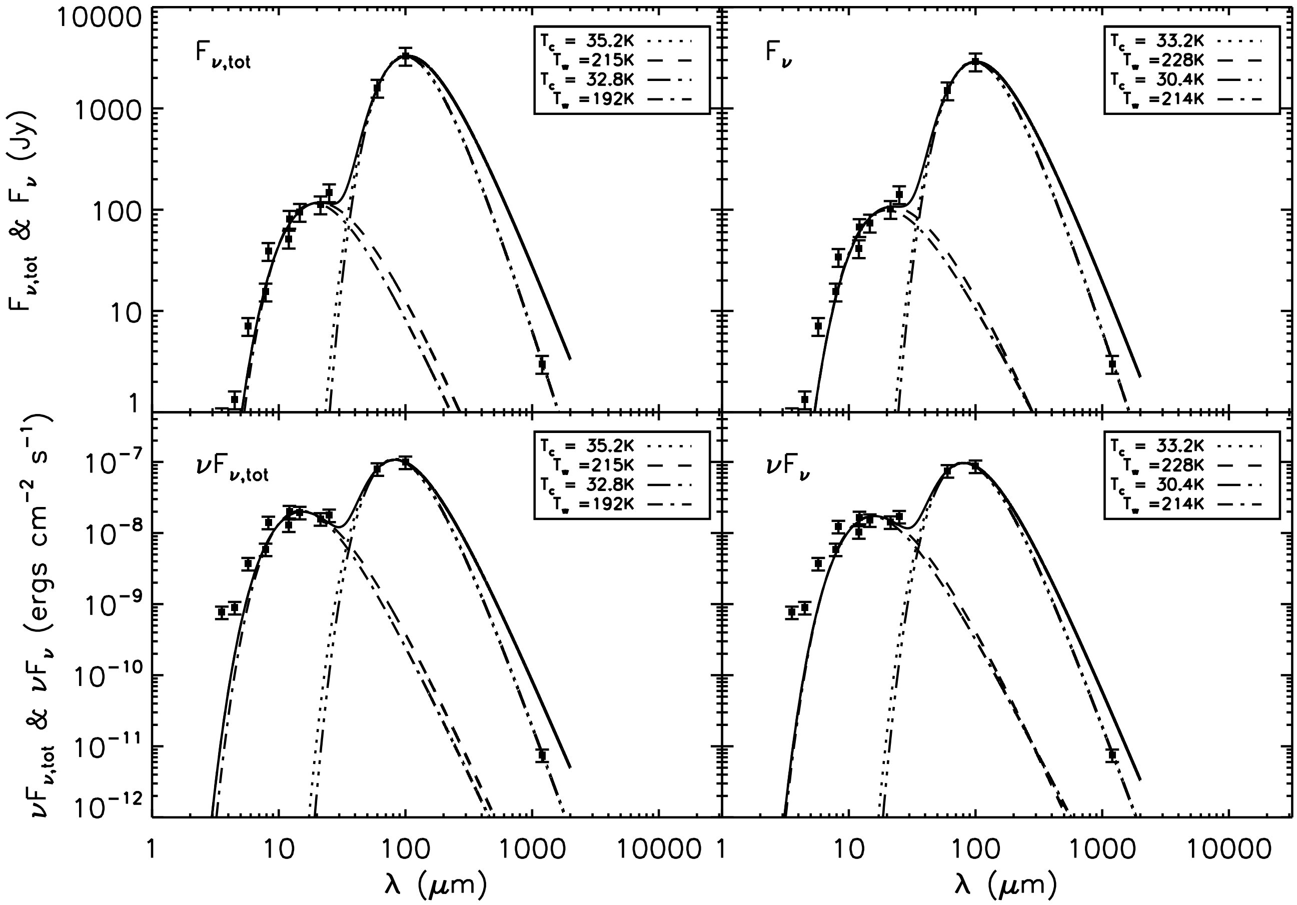

Fig. 1.— SED fitting results of BYF 73 (G286.2+0.2). *(a) Top left:* $F_{\nu,\rm tot}$ (no background subtracted); *(b) Top right:* F_ν (background subtracted); *(c) Bottom left:* $\nu F_{\nu,\rm tot}$ (no background subtracted); *(d) Bottom right:* νF_ν (background subtracted). The data in order of increasing wavelength are Spitzer-IRAC, MSX, IRAS, SIMBA. In the fiducial case, which is used for the main analysis of the 303 CHaMP clumps, we only use MSX and IRAS data to find colder component temperatures $T_c = 35.2, 33.2$ K (without and with background subtraction) (dotted lines) and $T_w = 215, 228$ K (dashed lines). The totals are shown by the solid lines. Fitting MSX, IRAS and the mm SIMBA flux leads to revised model fits with $T_c = 32.8, 30.4$ K (dash-dot-dot-dotted lines). Fitting IRAC, MSX and IRAS leads to revised model fits with $T_w = 192, 214$ K (dash-dotted lines). In both cases the bolometric fluxes change by $\lesssim 5\%$ from the fiducial case.

forming clumps in the sample (Barnes et al. 2010), as one example to show the effect of the mm flux measurement. The results from only the MSX and IRAS data are: $T_c = 35.2, 33.2$ K, $\beta_c = 1.45, 1.52$ and $\nu_0 = 101, 31.1$ THz, without and with background subtraction, respectively. Adding in the mm flux we now derive $T_c = 32.8, 30.4$ K, $\beta_c = 1.82, 1.78$ and $\nu_0 = 15.4, 11.1$ THz for these same cases. The bolometric flux, obtained by integrating over the model spectrum, changes from $(1.32, 1.22) \times 10^{-7}$ erg^{-1} s^{-1} cm^{-2}, without and with background subtraction respectively, to $(1.30, 1.20) \times 10^{-7}$ erg^{-1} s^{-1} cm^{-2} when the mm flux is utilized.

The fitting results for all 15 sources with mm flux measurements using the no background subtraction method are summarized in Table 1. These results show that T_c typically changes by $\lesssim 5$ K after including the mm flux. The mean value changes by about 10%. We find β_c changes from 2.0 ± 0.33 to 1.85 ± 0.41 after utilizing the mm flux. Most importantly, we find the bolometric fluxes, $F_{\rm tot}$ and F, typically change by $\lesssim 10\%$ after including the mm flux. Thus we conclude that the lack of longer wavelength data for the main sample only introduces a modest uncertainty of $\sim 10\%$ in $F_{\rm tot}$ and F. Note, however, that the limited FIR/sub-mm coverage of the SEDs, even with the SEST-SIMBA data, prevent accurate measurement of T_c, ν_0 and β. This situation will be improved with forthcoming data from the *Herschel* Hi-GAL survey (Molinari et al. 2010).

In this paper, we choose not to use the IRAC data for our fidicial SED fitting (although we do examine certain correlations of clump properties with the flux in the IRAC bands). The IRAC data are not available for about 10% of the CHaMP clumps (generally those furthest from the midplane) and we wish to maintain the same procedure for all the clumps in the sample. Furthermore, the bolometric luminosity is dominated by the colder component, even for clumps with the most active star formation (see, e.g. Fig. 1). For BYF 73, when we compare SED fitting (no background subtraction) with just MSX+IRAS to that with IRAC+MSX+IRAS we see: T_c changes from 35.1 K to

TABLE 1
Effect of 1.2 mm data on SED fitting.

BYF No.	T_c[a] (K)	$\log(F)$[a] (erg s^{-1} cm^{-2})	T_c[b] (K)	$\log(F)$[b] (erg s^{-1} cm^{-2})
73	35.2	−6.88	32.8	−6.89
126a	37.9	−5.64	37.9	−5.64
126b	35.2	−6.33	37.2	−6.33
126c	30.4	−6.39	31.8	−6.45
128a	36.4	−7.10	34.5	−7.04
128b	39.0	−5.80	39.9	−5.79
131b	37.0	−7.07	39.5	−7.06
131c	50.0	−6.46	41.4	−6.50
131d	39.6	−6.13	41.2	−6.13
131e	49.2	−6.32	42.7	−6.33
132d	37.0	−5.92	39.8	−5.89
132e	31.0	−6.68	37.5	−6.61
162	31.1	−8.46	33.5	−8.52
163a	40.1	−7.12	39.4	−7.12
163b	35.5	−7.48	39.2	−7.49

[a] using MSX and IRAS data
[b] using MSX, IRAS & mm data

35.0 K, T_w changes from 215 K to 230 K and F changes from 1.323×10^{-7} erg^{-1} s^{-1} cm^{-2} to 1.328×10^{-7} erg^{-1} s^{-1} cm^{-2}.

4. RESULTS

4.1. *HCO$^+$ Masses*

In this paper we set the clump mass, M, equal to that derived from analysis of HCO$^+$(1-0) emission, $M_{\rm col}$ (listed in column 9 of Table 5, Paper I). The distribution of these masses is presented in Fig. 2a. The masses range from $\sim 10-10^4\ M_\odot$. The clump masses (and other clump properties) are also listed in Table 2.

As discussed above, uncertainties in clump mass are likely to be at least a factor of 3 due to uncertainties in HCO$^+$ abundance, excitation temperature and clump distance. We expect relative clump masses are much more accurately determined, especially since a large fraction of the CHaMP clumps are in the Carina sprial arm, with about half in the same η Carinae giant molecular association at a common kinematic distance of $\sim$ 2.5 kpc.

4.2. *Bolometric Fluxes*

The bolometric flux distributions without, $F_{\rm tot}$ and with, F, background subtraction are presented in Fig. 2b. The mean 10σ sensitivity of the 4 IRAS bands are 0.7, 0.65, 0.85 and 3.0 Jy, which correspond to a bolometric flux of about 3×10^{-10} erg^{-1} s^{-1} cm^{-2} for a source with a typical angular size of 60″. This limit is also shown in Fig. 2b. We see that $F_{\rm tot}$ can be detected at better than 10σ for nearly all of the CHaMP clumps. We assume the uncertainty in $F_{\rm tot}$ is about 20% from the absolute flux calibration of the IR observations and about 10% from the two temperature greybody model fitting, i.e. adding in quadrature to about 22%.

For the faintest clumps, the total flux from the direction of the clump, $F_{\rm tot}$, can be similar to that of the background (i.e. the region surrounding the clump). The background subtracted flux, F_ν, can thus be very small (or even formally negative) at a particular wavelength. The uncertainty assigned to F_ν is of order the same level as the background. For deriving bolometric fluxes, the flux at 100μm is typically most important. Thus we flag those clumps that have a 100μm background flux that is > 0.75 times the clump flux, and consider these values of F, L and L/M to be highly uncertain, i.e. $\gtrsim$ 100% uncertainties.

4.3. *Bolometric Luminosities*

Given the clump distances from Paper I and our derived bolometric fluxes, we calculate the bolometric luminosities $L_{\rm tot}$ and L (without and with background subtraction, respectively). The distributions of $L_{\rm tot}$ and L are shown in Fig. 2c.

Adopting a typical distance uncertainty of 30%, we then estimate an uncertainty in $L_{\rm tot}$ of about 64%. L has somewhat greater uncertainty due to background flux estimation, and again we flag those sources where we expect this source of error dominates.

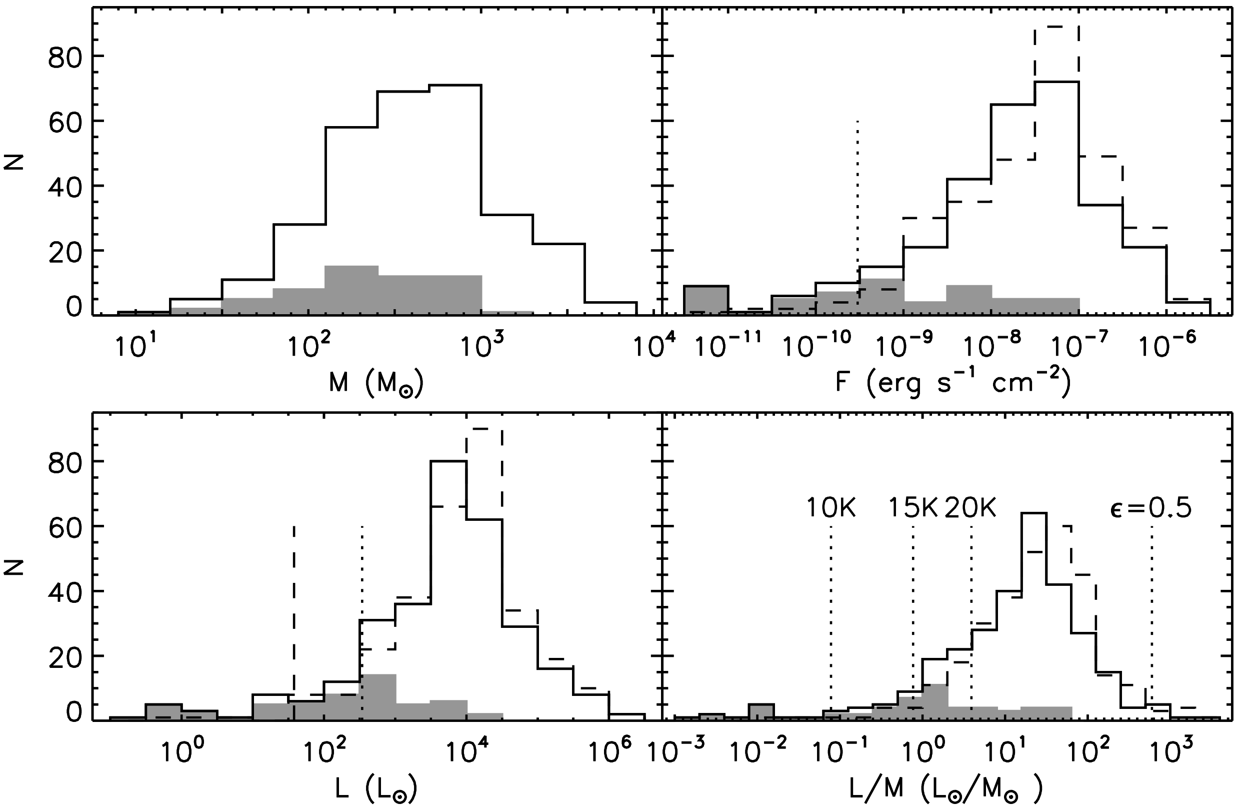

FIG. 2.— *(a) Top left:* Distribution of the masses (M, estimated from HCO$^+$(1-0)) of the 303 CHaMP clumps. The grey shaded histogram shows the sources for which the bolometric flux, F, measurements are uncertain due to background subtraction (see (b)). *(b) Top right:* Distribution of the bolometric fluxes (F, *solid line*, estimated from the 2 temperature greybody fit to the background subtracted SED; $F_{\rm tot}$, *dashed line*, estimated from the 2 temperature greybody fit to the total SED [no background subtracted]). The grey shaded histogram shows the sources for which the bolometric flux, F, measurements are uncertain due to having IRAS 100μm background fluxes > 0.75 of the clump flux). The vertical dotted line shows a bolometric flux of 3×10^{-10} erg^{-1} s^{-1} cm^{-2}, which is our estimate for the 10σ sensitivity flux limit of the IRAS data for a clump with typical angular size of 60″. *(c) Bottom left:* Distribution of bolometric luminosities (L, *solid line*, estimated from F; $L_{\rm tot}$, *dashed line*, estimated from $F_{\rm tot}$). The grey shaded histogram, a subset of L, shows the same sources as described in (b) with uncertain flux measurements due to background subtraction. The vertical dashed and dotted lines show the luminosity corresponding to the flux limit shown in (b) for clumps at 2.0 and 6.0 kpc, respectively. *(d) Bottom right:* Distribution of luminosity to mass ratios (L/M, *solid line*; $L_{\rm tot}/M$, *dashed line*). The grey shaded histogram, a subset of L/M, shows the same sources as described in (b) with uncertain flux measurements due to background subtraction. Three vertical dotted lines on the left side show $L/M = 0.078, 0.77, 3.9\ L_\odot/M_\odot$ (from left to right), which corresponds to a grey-body with $T = 10, 15, 20$ K. The vertical dotted line on the right side shows $L/M = 600\ L_\odot/M_\odot$, which corresponds a clump with an equal mass of gas and stars (i.e., a star formation efficiency $\epsilon \equiv M_*/(M_* + M) = 0.5$) that are on the ZAMS.

The mean luminosities are $\langle L_{\rm tot}\rangle = 5.2 \times 10^4 L_\odot$ and $\langle L\rangle = 4.2 \times 10^4 L_\odot$. For reference, this is about the luminosity of a 20 $M_\odot$ zero age main sequence (ZAMS) star (Schaller et al. 1992). The median value of L is $1.2 \times 10^4 L_\odot$: half of the sample are less luminous that a single 12 $M_\odot$ ZAMS star.

Note that the previous surveys of dust emission toward massive star forming regions by Mueller et al. (2002) and Faúndez et al. (2004) found $\langle L_{\rm tot}\rangle = 2.5 \times 10^5 L_\odot$ and $2.3 \times 10^5 L_\odot$, respectively. These values are much larger that those of the CHaMP clumps. We attribute this difference as being due to the different selection criteria of the samples: CHaMP is a complete sample of dense gas independent of star formation activity, while these other surveys were selected based on (massive) star formation indicators.

4.4. *Luminosity-to-mass ratios*

During the evolution of star-forming clumps, i.e. the formation of star clusters, the gas mass will decrease due to incorporation into stars and dispersal by feedback, causing the luminosity-to-mass ratio to increase. So L/M should be an evolutionary indicator of the star cluster formation process. The distribution of L/M is shown in Fig. 2d.

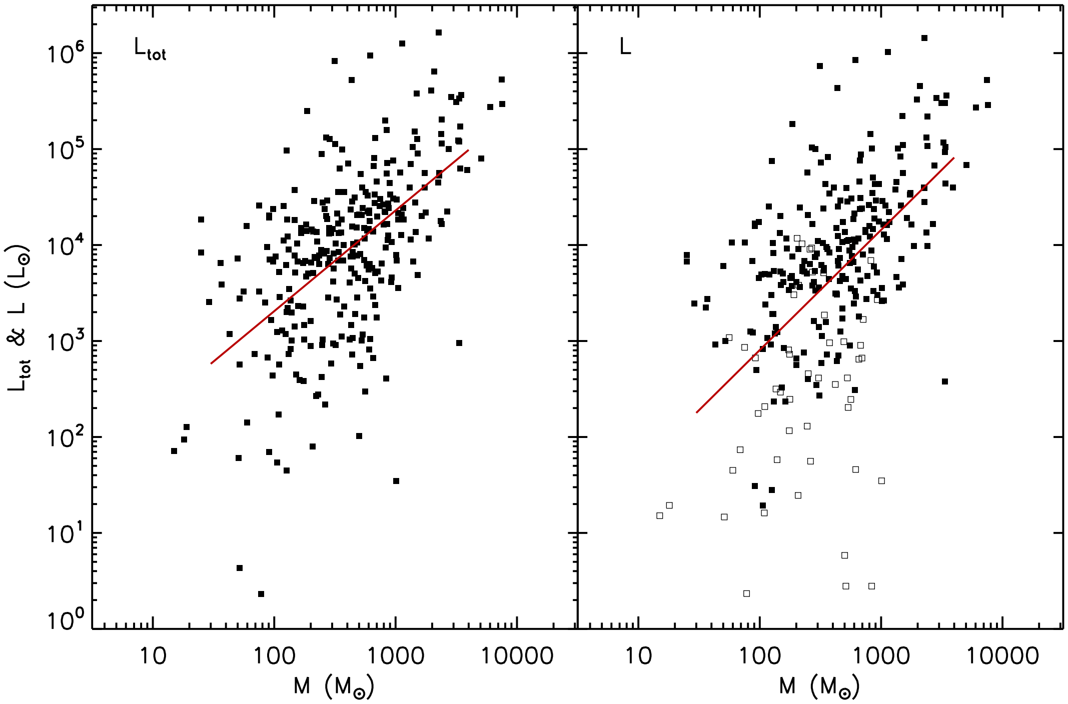

FIG. 3.— *(a) Left:* Correlation of $L_{\rm tot}$ with M, with best-fit relation $L_{\rm tot}/L_\odot = 16.2 \times (M/M_\odot)^{1.05}$ shown with a Spearman rank correlation coefficient 0.54 and 1.2×10^{-24} probability for a chance correlation. *(b) Right:* Correlation of L with M, with best-fit relation $L/L_\odot = 3.0 \times (M/M_\odot)^{1.25}$ shown with a Spearman rank correlation coefficient 0.55 and 7.2×10^{-25} probability for a chance correlation. Open squares show clumps with uncertain measurements of F due to IRAS 100μm background subtraction (see 2b).

Three dotted vertical lines at $L/M = 0.078, 0.77, 3.9\ L_\odot/M_\odot$ are used to show the values expected of clouds with dust temperatures of $T = 10, 15, 20$ K, which can be achieved in starless clumps via external heating. These values are calculated via

$$\frac{L/M}{L_\odot/M_\odot} = \frac{4\pi}{\Sigma}\int B_\nu(1-\exp(-\tau_\nu)\,{\rm d}\nu \rightarrow 0.0778\left(\frac{T}{10\,{\rm K}}\right)^{5.65}, \qquad (3)$$

where the latter evaluation is based on integrating the opacities of the Oseenkopf & Henning (1994) moderately-coagulated thin ice mantle dust model (and adopting a gas-to-dust mass ratio of 155) for clouds with $0.01 < \Sigma/{\rm g\,cm^{-2}} < 1$ and $10 < T/{\rm K} < 20$ (there is a modest dependence of L/M on $\Sigma^{0.02}$, which we ignore, normalizing the numerical factor of eq. (3 to $\Sigma = 0.03\,{\rm g\,cm^{-2}}$, typical of the CHaMP clump sample). Values of $L/M \sim 1 L_\odot/M_\odot$ are thus expected to define the lower end of the L/M distribution, as is observed.

To understand the upper end of the observed distribution, consider a clump with an equal mass of gas and stars that are on the zero age main sequence (ZAMS). For a Salpeter IMF down to $0.1 M_\odot$, this will have $L/M \sim 600 L_\odot/M_\odot$ (Leitherer et al. 1999; Tan & McKee 2002). Other IMFs typically considered for Galactic star-forming regions give similar numbers to within about a factor of two. This value is close to the upper end of the distribution of L/M shown in Fig. 2d. Note that as the gas mass goes to very small values, L/M should rise far above $600 L_\odot/M_\odot$. However, in this case a smaller fraction of the bolometric luminosity will be re-radiated in the MIR and FIR, and so would be missed by our analysis. Also such "revealed" clusters with small amounts of dense gas would not tend to be objects in the CHaMP sample, which is complete only on the basis of emission of dense gas tracers.

To investigate the relation between bolometric luminosity and gas mass, we also show the correlation between $L_{\rm tot}$ and M in Fig. 3a and the correlation between L and M in Fig. 3b. The best-fit power law results are as follows:

$$L_{\rm tot}/L_\odot = 16.2(\pm 9.5) \times (M/M_\odot)^{1.05\pm 0.09} \qquad (4)$$

with Spearman rank correlation coefficient 0.54 and 1.2×10^{-24} probability for a chance correlation for non-background subtraction method and

$$L/L_\odot = 3.0(\pm 1.8) \times (M/M_\odot)^{1.25\pm 0.11} \qquad (5)$$

with Spearman rank correlation coefficient 0.55 and 7.2×10^{-25} probability for a chance correlation for the background subtraction method. Both have shown significant positive correlations. The more massive the clump is, the more luminous it tends to be.

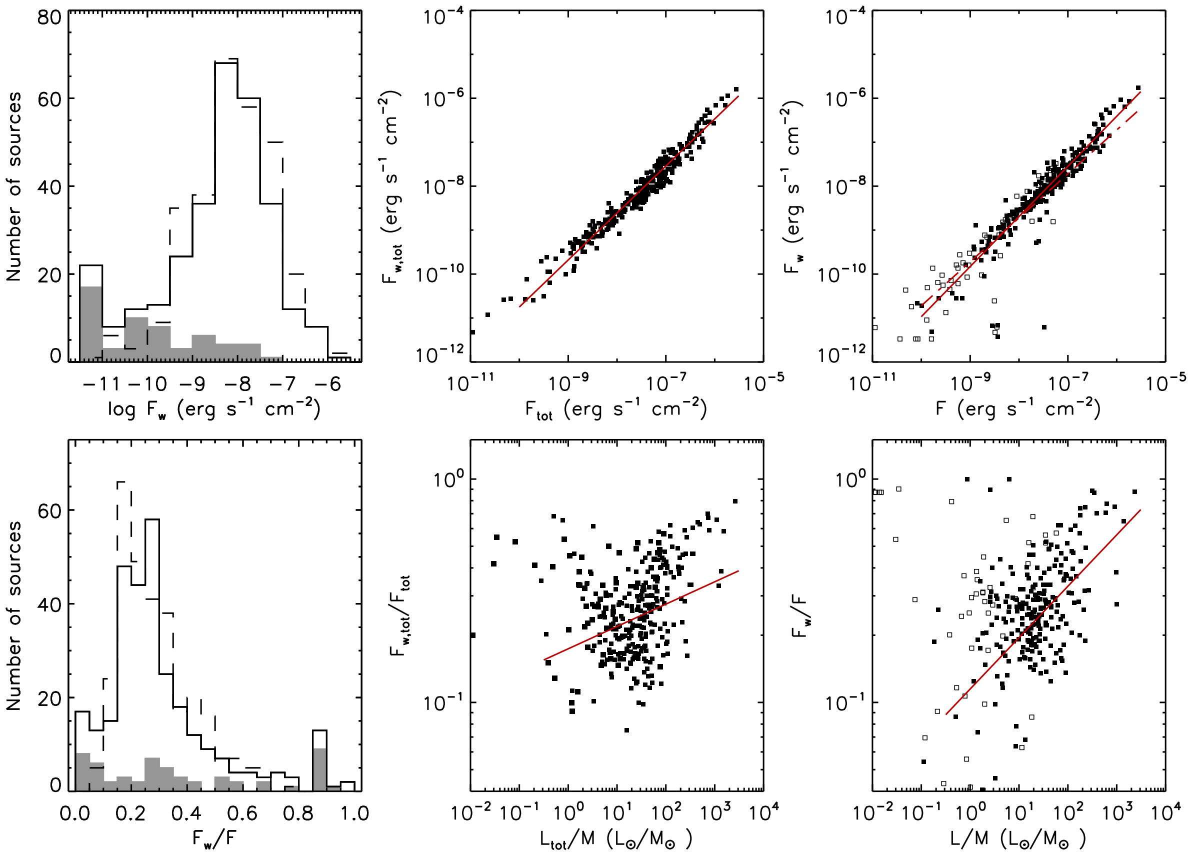

Fig. 4.— *(a) Top left:* Distributions of F_w (solid line) and $F_{w,\rm tot}$ (dashed line). The shaded histogram shows the sources for which the bolometric flux, F, measurements are uncertain due to background subtraction (see Fig. 2.). *(b) Top middle:* Correlation of $F_{w,\rm tot}$ with $F_{\rm tot}$, with a best-fit relation of $F_{w,\rm tot} = 0.89 \times F_{\rm tot}^{1.08}$ with a Spearman rank correlation coefficient 0.98 and a negligible probability for a chance correlation. *(c) Top right:* Correlation of F_w with F, with two best-fit relations shown $F_{\rm w} = 2.69(\pm 1.25) \times F^{1.14\pm0.02}$ (solid line) and $F_{\rm w} = 0.30(\pm 0.01) \times F$ (dashed line). Open squares show clumps with uncertain measurements of F due to IRAS 100μm background subtraction (see 2b). *(d) Bottom left:* Distribution of F_w/F (solid line) and $F_{w,\rm tot}/F_{\rm tot}$ (dashed line), with shaded sources as in (a). *(e) Bottom middle:* Correlation of $F_{w,\rm tot}/F_{\rm tot}$ with $L_{\rm tot}/M$, with best-fit relation $F_{w,\rm tot}/F_{\rm tot} = 0.19 \times (L_{\rm tot}/M/[L_\odot/M_\odot])^{0.10}$ shown with Spearman rank correlation coefficient 0.29 and 4.3×10^{-7} probability for a chance correlation. *(f) Bottom right:* Correlation of F_w/F with L/M, with best-fit relation $F_{\rm w}/F = 0.11 \times (L/M/[L_\odot/M_\odot])^{0.23}$ shown with a Spearman rank correlation coefficient 0.43 and 2.5×10^{-12} probability for a chance correlation. As star cluster formation proceeds to higher values of L/M, the warmer component becomes more important.

The mean, median and standard deviation of $\log(L_{\rm tot}/M/[L_\odot/M_\odot])$ are 1.34, 1.43 and 0.77 respectively for non-background subtraction method. For the background subtraction method, the mean, median and standard deviation of $\log(L/M/[L_\odot/M_\odot])$ are 1.06, 1.25 and 0.97 respectively.

Molinari et al. (2008) have studied the SEDs of 42 potentially massive individual young stellar objects (YSOs). By fitting the SEDs with YSOs models they obtained the bolometric luminosity and envelope mass, $M_{\rm env}$. They presented the $L_{\rm bol} - M_{\rm env}$ diagram as a tool to diagnose the pre-MS evolution of massive YSOs. For their sample, the mean, median and standard deviation of $\log(L/M)$ are 1.91, 1.77 and 0.66 respectively. This illustrates the different nature of their sample: objects that are already forming massive stars and with much higher values of L/M. However, we caution that systematic differences could also arise because of the different methods being used to derive masses (i.e. $\rm HCO^+$ versus mm flux-based masses).

Similarly, Mueller et al. (2002), Beuther et al. (2002) and Faúndez et al. (2004) reported mean values of $\log(L/M)$ as 2.04 ± 0.34, 1.18 ± 0.34 and 1.75 ± 0.38. Note here that in Beuther et al. (2002) they have used opacity from Hildebrand (1983), which is 4.9 times smaller than the opacity from Ossenkopf & Henning (1994) used in Mueller et al. (2002) and Faúndez et al. (2004). So the mass derived in Beuther et al. (2002) would be 4.9 times smaller and their mean $\log(L/M)$ will be 1.87 ± 0.34 if they adopt the opacity from Ossenkopf & Henning (1994).

4.5. *The Warm Component*

From the two temperature fitting process, we derived the total, $F_{\rm w,tot}$, and background-subtracted, $F_{\rm w}$, flux for the warm component. The distributions of $F_{\rm w,tot}$ and $F_{\rm w}$ are shown in Fig. 4a. The correlation of $F_{\rm w,tot}$ with $F_{\rm tot}$ is shown in Fig. 4b, and that of $F_{\rm w}$ with F in Fig. 4c. These both show significant correlations. We derive a best-fit power law for the data (e.g. Kelly 2007), finding

$$F_{\rm w,tot} = 0.89(\pm 0.35) \times F_{\rm tot}^{1.08\pm 0.02}. \tag{6}$$

For the background subtracted case, which we consider to be the most accurate measure of the intrinsic properties of the clumps, we try two different constrained fits, finding:

$$F_{\rm w} = 2.69(\pm 1.25) \times F^{1.14\pm 0.02} \tag{7}$$

$$F_{\rm w} = 0.30(\pm 0.01) \times F \tag{8}$$

The distributions of $F_{\rm w,tot}/F_{\rm tot}$ and $F_{\rm w}/F$ are shown in Fig. 4d. The warm component flux generally accounts for $10\% - 30\%$ of the total flux, so F_w and F are not independent, which can contribute to these correlations.

To investigate if there are any systematic trends associated with the warm component during star cluster formation as measured by the clump luminosity to mass ratio, we show the correlation of $F_{\rm w,tot}/F_{\rm tot}$ versus $L_{\rm tot}/M$ in Fig. 4e and F_w/F versus L/M in Fig. 4f.

The power law fit results of this positive correlation are as follows:

$$F_{\rm w,tot}/F_{\rm tot} = 0.19(\pm 0.03) \times (L_{\rm tot}/M/[L_\odot/M_\odot])^{0.10\pm 0.03} \tag{9}$$

and

$$F_{\rm w}/F = 0.11(\pm 0.02) \times (L/M/[L_\odot/M_\odot])^{0.23\pm 0.02} \tag{10}$$

The Spearman rank correlation coefficients (see Fig. 4) indicates a positive correlation exists in both cases.

Our findings support the idea that as stars gradually form in molecular clumps and the luminosity-to-mass ratio increases, a larger fraction of the bolometric flux will emerge at shorter wavelengths. This result can provide a constraint on theoretical radiative transfer models of star cluster formation.

4.6. *The Hot (IRAC Band) Component*

We now search for any correlation of the IRAC band flux, which extends from $\sim 3 - 9\ \mu$m, with the bolometric flux and the luminosity to mass. These relatively short wavelengths are more sensitive to hot dust directly heated by embedded young stars. We first measure the total IRAC band flux using a simple trapezoidal rule integration in the four IRAC bands, without background subtraction, $F_{\rm IRAC,tot}$, and then attempt to subtract the background to derive $F_{\rm IRAC}$.

The distributions of $F_{\rm IRAC,tot}$ and $F_{\rm IRAC}$ are shown in Fig. 5a. The correlation of $F_{\rm IRAC,tot}$ with $F_{\rm tot}$ is shown in Fig. 5b, and that of $F_{\rm IRAC}$ with F in Fig. 5c. These both show significant correlations. The power law fit results of these two correlations are as follows:

$$F_{\rm IRAC,tot} = 3.1(\pm 1.7) \times 10^{-3} \times F_{\rm tot}^{0.84\pm 0.03} \tag{11}$$

and, trying two constrained fits,

$$F_{\rm IRAC} = 4.0(\pm 3.0) \times 10^{-3} \times F^{0.87\pm 0.04} \tag{12}$$

$$F_{\rm IRAC} = 5.1(\pm 0.6) \times 10^{-2} \times F. \tag{13}$$

The distributions of $F_{\rm IRAC,tot}/F_{\rm tot}$ and $F_{\rm IRAC}/F$ are shown in Fig. 5d. The IRAC component flux generally accounts for $\sim 1\% - 10\%$ of the total flux, so $F_{\rm IRAC}$ and F are essentially independent, unlike for F_w (above).

To investigate if there are any systematic trends associated with the IRAC (hot) component during star cluster formation as measured by the clump luminosity to mass ratio, we show the correlation of $F_{\rm IRAC,tot}/F_{\rm tot}$ versus $L_{\rm tot}/M$ in Fig. 5e and $F_{\rm IRAC}/F$ versus L/M in Fig. 5f. The best-fit power law relations are as follows:

$$F_{\rm IRAC,tot}/F_{\rm tot} = 0.11(\pm 0.01) \times (L_{\rm tot}/M/[L_\odot/M_\odot])^{-0.28\pm 0.02}. \tag{14}$$

The Spearman rank correlation coefficient of $F_{\rm IRAC,tot}/F_{\rm tot}$ versus $L_{\rm tot}/M$ is negative. We expect this is due to the fact that $F_{\rm tot}$ and $L_{\rm tot}$ are correlated, while $F_{\rm IRAC,tot}$ is often dominated by "background" (i.e. both background and foreground, i.e. unrelated) emission.

The result for $F_{\rm IRAC}/F$ versus L/M is

$$F_{\rm IRAC}/F = 0.02(\pm 0.002) \times (L/M/[L_\odot/M_\odot])^{0.02\pm 0.05}, \tag{15}$$

so from this there is no evidence for an increase in the hot component as cluster evolution (as measured by L/M) proceeds. As the luminosity input into the clump rises, a fairly constant fraction emerges in the IRAC bands. Again, this result can provide a constraint on theoretical models of star cluster formation.

In order to more directly probe the evolution of IRAC-traced hot dust emission and its possible correlation with luminosity to mass ratio, we also calculated the IRAC band specific intensity without, $I_{\rm IRAC,tot}$ and with, $I_{\rm IRAC}$

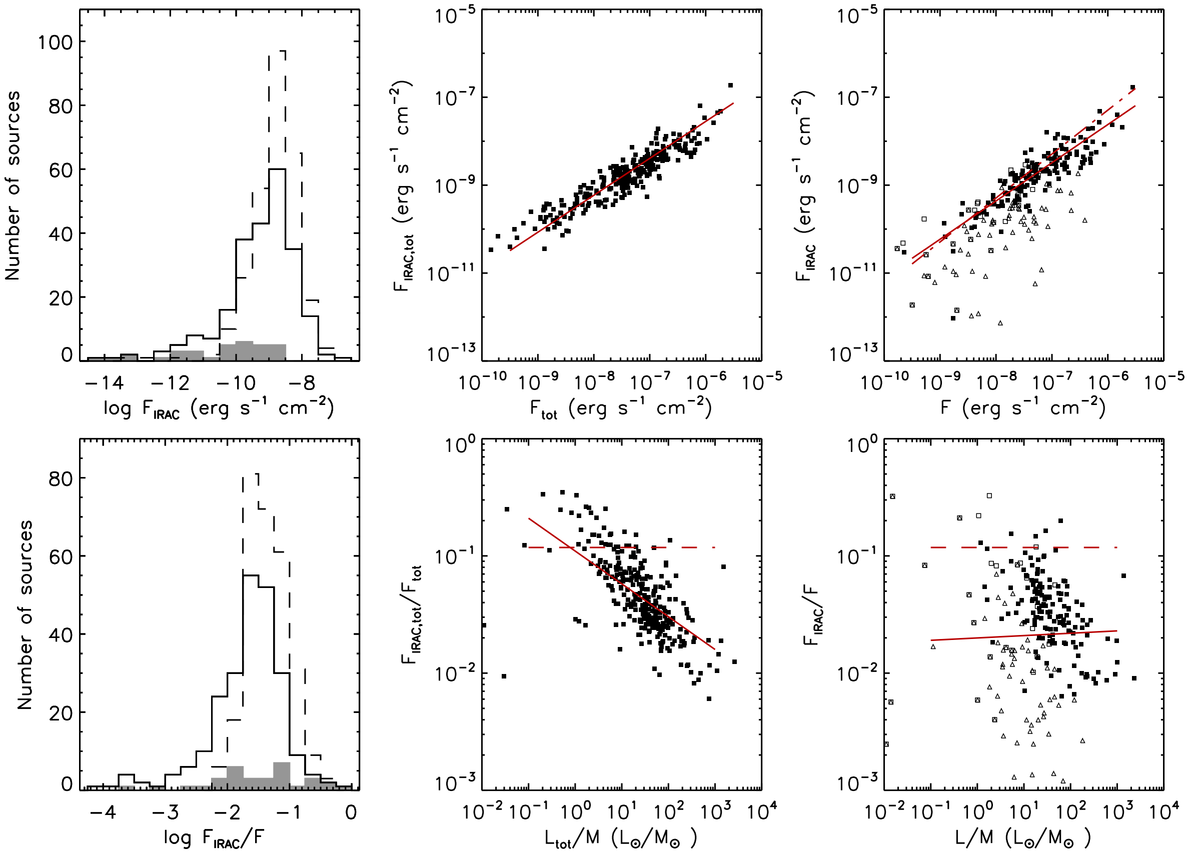

FIG. 5.— *(a) Top left:* Distributions of $F_{\rm IRAC}$ (solid line) and $F_{\rm IRAC,tot}$ (dashed line). The shaded histogram shows the sources for which the bolometric flux, F, measurements are uncertain due to background subtraction (see Fig. 2). *(b) Top middle:* Correlation of $F_{\rm IRAC,tot}$ with $F_{\rm tot}$, with a best-fit relation of $F_{\rm IRAC,tot} = 3.1 \times 10^{-3} F_{\rm tot}^{0.84}$. The Spearman rank correlation coefficient is 0.91 and corresponding to a negligible probability of chance correlation. *(c) Top right:* Correlation of $F_{\rm IRAC}$ with F, with two best-fit relations shown: $F_{\rm IRAC} = 4.0(\pm3.0) \times 10^{-3} \times F^{0.87\pm0.04}$ (solid line) and $F_{\rm IRAC} = 5.1(\pm0.6) \times 10^{-2} \times F$ (dashed line). Open squares show clumps with uncertain measurements of F due to IRAS 100μm background subtraction (see 2b). Open triangles show clumps with uncertain measurements of $F_{\rm IRAC}$ due to IRAC 8μm background subtraction. *(d) Bottom left:* Distribution of $F_{\rm IRAC}/F$ (solid line) and $F_{\rm IRAC,tot}/F_{\rm tot}$ (dashed line), with shaded sources as in (a). *(e) Bottom middle:* Correlation of $F_{\rm IRAC,tot}/F_{\rm tot}$ with $L_{\rm tot}/M$, with a best-fit relation of $F_{\rm IRAC,tot}/F_{\rm tot} = 0.11(\pm0.01) \times (L_{\rm tot}/M/[L_\odot/M_\odot])^{-0.28\pm0.02}$ The Spearman rank correlation coefficient is -0.69 and corresponding to a negligible probability for a chance correlation. The horizontal dashed line corresponds to 0.11, which is the $F_{\rm IRAC}/F$ ratio of the dust emission from the diffuse interstellar medium and is calculated using the data from Li & Draine (2001). *(f) Bottom right:* Correlation of $F_{\rm IRAC}/F$ with L/M, with a best-fit relation of $F_{\rm IRAC,tot}/F_{\rm tot} = 0.02(\pm0.002) \times (L/M/[L_\odot/M_\odot])^{0.02\pm0.05}$. The Spearman rank correlation coefficient is -0.14 and corresponding to 0.05 probability for a chance correlation.

background subtraction (Fig. 6). Note that both the specific intensities and the luminosity to mass ratios are essentially independent of distance uncertainties. The best-fit relations are as follows:

$$I_{\rm IRAC,tot} = 3.0(\pm0.5) \times 10^{-4} \times (L_{\rm tot}/M/[L_\odot/M_\odot])^{0.71(\pm0.05)}\ {\rm erg\ s^{-1}\ cm^{-2}\ sr^{-1}} \tag{16}$$

with Spearman rank correlation coefficient 0.57 and 10^{-13} probability for a chance correlation, and, trying two constrained fits,

$$I_{\rm IRAC} = 3.0(\pm0.7) \times 10^{-5} \times (L/M/[L_\odot/M_\odot])^{1.05(\pm0.05)}\ {\rm erg\ s^{-1}\ cm^{-2}\ sr^{-1}} \tag{17}$$

$$I_{\rm IRAC} = 5.0(\pm1.9) \times 10^{-5} \times (L/M/[L_\odot/M_\odot])\ {\rm erg\ s^{-1}\ cm^{-2}\ sr^{-1}}. \tag{18}$$

The former has a Spearman rank correlation coefficient 0.66 and 10^{-19} probability for a chance correlation.

Thus the IRAC band specific intensity, which is essentially independent of L/M (since only a very small fraction of L emerges at these wavelengths) and more directly traces embedded stellar populations, has a significant correlation with L/M, thus validating the use of L/M as an evolutionary indicator of star cluster formation. The specific functional form of the correlation is a constraint on radiative transfer models of star cluster formation.

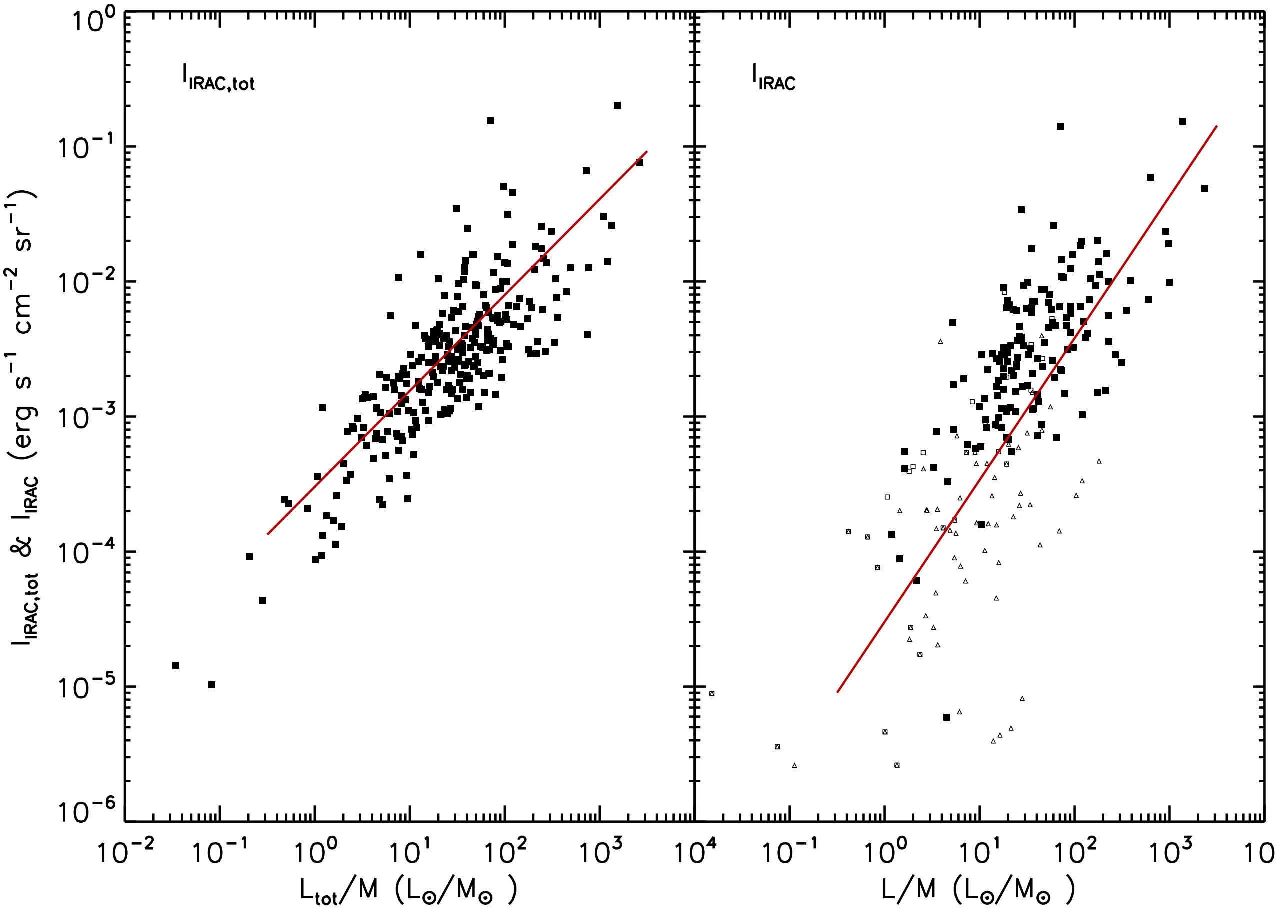

FIG. 6.— *(a) Left:* Correlation of $I_{\rm IRAC,tot}$ with $L_{\rm tot}/M$, with a best-fit relation of $I_{\rm IRAC,tot} = 3.0(\pm0.5)\times10^{-4}\times(L_{\rm tot}/M/[L_\odot/M_\odot])^{0.71(\pm0.05)}$ with a Spearman rank correlation coefficient 0.57 and negligible probability for a chance correlation. *(b) Right:* Correlation of $I_{\rm IRAC}$ with L/M, with a best-fit relation of $I_{\rm IRAC} = 3.0(\pm0.7)\times10^{-5}\times(L/M/[L_\odot/M_\odot])^{1.05(\pm0.05)}$ with a Spearman rank correlation coefficient 0.66 and negligible probability for a chance correlation. Open squares show clumps with uncertain measurements of F due to IRAS 100μm background subtraction (see 2b). Open triangles show clumps with uncertain measurements of $F_{\rm IRAC}$ due to IRAC 8μm background subtraction.

The near linear relation of $I_{\rm IRAC}$ with L/M (although with large scatter, to be expected from IMF sampling) suggests that $I_{\rm IRAC}$ also has a near linear dependence on embedded stellar content relative to gas mass, i.e. the instantaneous star formation efficiency, $\epsilon' \equiv M_*/M$, which, note, is normalized by the gas mass. (We define $\epsilon \equiv M_*/(M_* + M)$, which becomes similar to ϵ' when $\epsilon' \ll 1$.) Thus, for a Salpeter IMF down to $0.1M_\odot$ (see §4.4),

$$\epsilon' \simeq 1.0\frac{L/M}{600L_\odot/M_\odot} \simeq 0.33(\pm0.16)\frac{I_{\rm IRAC}}{10^{-2}\ {\rm erg\ s^{-1}\ cm^{-2}\ sr^{-1}}}, \tag{19}$$

where we have used the numerical result of the constrained linear fit (eq. 18). This may be a useful relation for estimating star formation efficiencies of statistical samples of star-forming clumps (at least those with similar densities to local Galactic clumps), when only IRAC data are available and a background subtraction can be performed.

4.7. *Cold Component Dust Temperature and Bolometric Temperature*

We now search for any correlation of the cold component dust temperature, $T_{\rm c,tot}$ (based on total fluxes with no background subtracted) and T_c (based on fluxes after background subtraction), with the luminosity to mass ratio. We note that the available data for the clumps generally are limited at long wavelengths to the IRAS 100 μm data and so our accuracy for estimating T_c is limited to about ±5 K (see §3.2).

The distributions of $T_{\rm c,tot}$ and T_c are shown in Fig. 7a. The mean values are $\langle T_{\rm c,tot}\rangle = 33\pm5$ K and $\langle T_{\rm c}\rangle = 33\pm7$ K. These results are similar to those derived in other surveys, such as: $\langle T\rangle = 29\pm9$ K in the large sample of Mueller et al. (2002); $\langle T\rangle = 45\pm11$ K in the large sample of Sridharan et al. (2002); $\langle T\rangle = 32\pm5$ K in the sample of Molinari et al. (2000); $\langle T\rangle = 35\pm6$ K in the sample of Hunter et al. (2000); $\langle T\rangle = 30$K in the sample of Molinari et al. (2008); and $\langle T\rangle = 32$K in the sample of Faúndez et al. (2004).

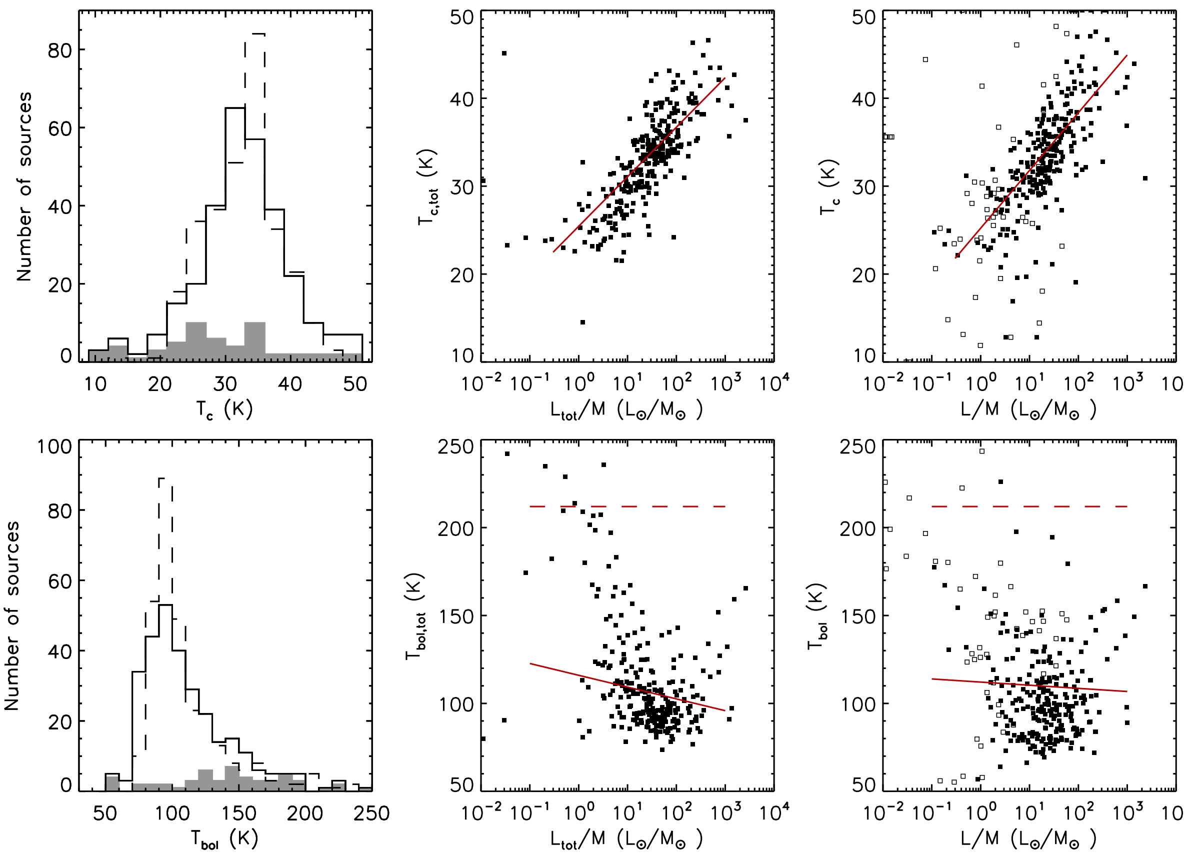

FIG. 7.— *(a) Top left:* Distribution of T_c (solid line) and $T_{c,\rm tot}$ (dashed line). The shaded histogram shows the sources for which the bolometric flux, F, measurements are uncertain due to background subtraction (see Fig. 2). *(b) Top middle:* Correlation of $T_{c,\rm tot}$ with $L_{\rm tot}/M$, with a best-fit relation of $T_{c,\rm tot}/{\rm K} = 5.6(\pm 0.5) \times \log(L_{\rm tot}/M/[L_\odot/M_\odot]) + 25.4(\pm 0.8)$, a Spearman rank correlation coefficient 0.81 and negligible probability for a chance correlation. *(c) Top right:* Correlation of T_c with L/M, with a best-fit relation of $T_c/{\rm K} = 6.6(\pm 0.6) \times \log(L/M/[L_\odot/M_\odot]) + 25.2(\pm 1.0)$ with a Spearman rank correlation coefficient 0.65 and 4.8×10^{-38} probability for a chance correlation. Open squares show clumps with uncertain measurements of F due to IRAS 100μm background subtraction (see 2b). *(d) Bottom left:* Distribution of $T_{\rm bol}$ (solid line) and $T_{\rm bol,tot}$ (dashed line). The shaded histogram shows the sources for which the bolometric flux, F, measurements are uncertain due to background subtraction (see Fig. 2). *(e) Bottom middle:* Correlation of $T_{\rm bol,tot}$ with $L_{\rm tot}/M$, with a best-fit relation of $T_{\rm bol,tot}/{\rm K} = -6.7(\pm 3.4) \times \log(L_{\rm tot}/M/[L_\odot/M_\odot]) + 116.0(\pm 6.4)$ with a Spearman rank correlation coefficient -0.15 and 0.06 probability for a chance correlation. The horizontal dashed line represents $T = 210$ K, which is the bolometric temperature of the dust emission in the diffuse ISM calculated using the data from Li & Draine (2001). *(f) Bottom right:* Correlation of $T_{\rm bol}$ with L/M, a best-fit relation of $T_{\rm bol}/{\rm K} = -1.8(\pm 3.3) \times \log(L/M/[L_\odot/M_\odot]) + 112.1(\pm 3.3)$ with a Spearman rank correlation coefficient -0.15 and 0.06 probability for a chance correlation.

The correlation of $T_{c,\rm tot}$ with $L_{\rm tot}/M$ is shown in Fig. 7b and that of $T_{\rm c}$ with L/M in Fig. 7c. We see clear positive correlations are present — the temperature rises as L/M increases. We find best-fit relations:

$$T_{c,\rm tot}/{\rm K} = 5.6(\pm 0.5) \times \log(L_{\rm tot}/M/[L_\odot/M_\odot]) + 25.4(\pm 0.8) \tag{20}$$

with Spearman rank correlation coefficient 0.81 and negligible probability for a chance correlation, and

$$T_c/{\rm K} = 6.6(\pm 0.6) \times \log(L/M/[L_\odot/M_\odot]) + 25.2(\pm 1.0) \tag{21}$$

with Spearman rank correlation coefficient 0.65 and negligible probability for a chance correlation.

"Bolometric temperature", $T_{\rm bol}$, has been proposed as a measure of the evolutionary development of a young stellar object (YSO) (Ladd et al. 1991; Myers & Ladd 1993; Myers et al. 1998). It is the temperature of a blackbody having the same weighted mean frequency as the observed SED. As the envelopes in those YSO systems are dispersed, their bolometric temperatures will rise. This is because the FIR emission decreases while the NIR and MIR emission increases.

We calculated the bolometric temperature for our molecular clumps following Myers & Ladd (1993):

$$T_{\rm bol} = 1.25 \times 10^{-11} \langle \nu \rangle \ \ {\rm K\,Hz^{-1}} \tag{22}$$

where $\langle \nu \rangle \equiv \int_0^\infty \nu F_\nu d\nu / \int_0^\infty F_\nu d\nu$ is the flux weighted mean frequency. The coefficient of $\langle \nu \rangle$ in eq. (22) is chosen so that a blackbody emitter at temperature T has $T_{\rm bol} = T$.

The distributions of $T_{\rm bol,tot}$ (based on total fluxes with no background subtraction) and $T_{\rm bol}$ (based on fluxes after background subtraction) are shown in Fig. 7d. These have mean values 92 ± 18 K and 113 ± 44 K, respectively. For comparison, Mueller et al. (2002) find a mean value of 78 ± 21 K for their sample.

The correlation of $T_{\rm bol,tot}$ with $L_{\rm tot}/M$ is shown in Fig. 7e and that of $T_{\rm bol}$ with L/M in Fig. 7f. We find best-fit relations:

$$T_{\rm bol,tot}/{\rm K} = -6.7(\pm 3.4) \times \log(L_{\rm tot}/M/[L_\odot/M_\odot]) + 116.0(\pm 6.4) \tag{23}$$

with Spearman rank correlation coefficient -0.15 and 0.06 probability for a chance correlation, and

$$T_{\rm bol}/{\rm K} = -1.8(\pm 3.3) \times \log(L/M/[L_\odot/M_\odot]) + 112.1(\pm 3.3) \tag{24}$$

with Spearman rank correlation coefficient -0.15 and 0.06 probability for a chance correlation.

Especially for $T_{\rm bol}$, where background effects have been subtracted, we do not find evidence for a significant correlation. We suspect this is because the uncertainties in deriving $T_{\rm bol}$ are relatively large compared to the expected size of any trend for $T_{\rm bol}$ to increase during star cluster formation. This is in contrast to the measures F_w/F and $I_{\rm IRAC}$, which show clear changes by about a factor of 10 or more as L/M increases.

5. DISCUSSION

5.1. *Dependence of L and L/M on Mass Surface Density, Σ*

Consider a clump that forms stars at a fixed efficiency per free-fall time, $\epsilon_{\rm ff}$. The overall accretion rate to stars is

$$\dot{M}_* = \epsilon_{\rm ff}\frac{M}{t_{\rm ff}} = \frac{(8G)^{1/2}}{\pi^{1/4}}\epsilon_{\rm ff}(M\Sigma)^{3/4} = 2.92 \times 10^{-4}\frac{\epsilon_{\rm ff}}{0.02}\left(\frac{M}{10^3\,M_\odot}\frac{\Sigma}{\rm g\,cm^{-2}}\right)^{3/4} M_\odot\,{\rm yr}^{-1}, \tag{25}$$

where we have normalized to a value of $\epsilon_{\rm ff}$ estimated by Krumholz & Tan (2007). Then the accretion luminosity is

$$L_{\rm acc} = f_{\rm acc}\frac{G\dot{M}_*\bar{m}_*}{\bar{r}_*} = 2270 f_{\rm acc}\frac{\bar{m}_*}{M_\odot}\frac{4R_\odot}{\bar{r}_*}\frac{\epsilon_{\rm ff}}{0.02}\left(\frac{M}{10^3\,M_\odot}\frac{\Sigma}{\rm g\,cm^{-2}}\right)^{3/4} L_\odot. \tag{26}$$

Here $f_{\rm acc}$ is the fraction of the accretion power that is radiated. While for individual protostars we expect $f_{\rm acc} \sim 0.5$ because of the mechanical luminosity of protostellar outflows, in early-stage star-forming clumps much of the outflow kinetic energy is likely to be liberated via radiative shocks and thus contribute to the total clump luminosity. Thus we adopt $f_{\rm acc} = 1$ as a fiducial value. In the above equation, $\bar{m}_*$ is the mean protostellar mass, weighted by accretion energy release. For a Salpeter IMF from 0.1 to 120 $M_\odot$, the mean stellar mass is 0.353 $M_\odot$, while the mean gravitational energy is $2.06 G M_\odot^2/\bar{r}_*$, assuming $\bar{r}_*$ is independent of m_* (discussed below). For accretion near the end of individual star formation, this implies $\bar{m}_* \simeq 1.4 M_\odot$, however the typical unit of accretion energy release will be when the protostar has $2^{-1/2}$ of its final mass. Thus we estimate $\bar{m}_* \simeq 1 M_\odot$ as a typical fiducial value in eq. (26).

The protostellar evolution models of Tan & McKee (2002), developed for protostars forming with accretion rates appropriate for cores fragmenting from a clump with $\Sigma \simeq 1\,{\rm g\,cm^{-2}}$ (see also Stahler 1988; Palla & Stahler 1992; Nakano et al. 2000; McKee & Tan 2003), indicate that the sizes of all protostars are close to ~ 3 to $4 R_\odot$ when their masses are $\lesssim 1 M_\odot$. After this the size increases along the deuterium core burning sequence, reaching about $6\,R_\odot$ by the time the protostars have $1.5\,M_\odot$. After this, sizes stay relatively constant until $m_* \sim 5\,M_\odot$. Given these relatively modest changes in r_* with m_*, we adopt a fiducial value of $\bar{r}_* = 4\,R_\odot$ in eq. (26).

We can now use eqs. (26) and (3) to estimate minimum values of L/M for star-forming clumps. We have

$$\frac{L_{\rm min}/M}{L_\odot/M_\odot} = 0.77\left(\frac{T}{15\,{\rm K}}\right)^{5.65} + \frac{L_{\rm acc}/M}{L_\odot/M_\odot} \tag{27}$$

$$= 0.77\left(\frac{T}{15\,{\rm K}}\right)^{5.65} + 2.27 f_{\rm acc}\frac{\bar{m}_*}{M_\odot}\frac{4R_\odot}{\bar{r}_*}\frac{\epsilon_{\rm ff}}{0.02}\left(\frac{M}{10^3\,M_\odot}\right)^{-1/4}\left(\frac{\Sigma}{\rm g\,cm^{-2}}\right)^{3/4}, \tag{28}$$

where T is the dust temperature expected from ambient heating of starless clumps. Note that because of internal stellar luminosities that will contribute in addition to $L_{\rm acc}$, $L_{\rm min}/M$ provides only a lower bound on the distribution of L/M of star-forming clumps.

In Fig. 8a and b, we plot the dependence of $L_{\rm tot}$ and L with Σ. Note Σ, like M, is based on the HCO$^+$ observations and analysis. We estimate Σ as $M/2$ divided by the projected area of the FWHM ellipse of Paper I. This will give a value of Σ for the typical mass element in the clump. We find best-fit relations:

$$L_{\rm tot} = 3.15(\pm 1.33) \times 10^5 \times (\Sigma/{\rm g\,cm^{-2}})^{1.03\pm 0.15}\,L_\odot \tag{29}$$

with Spearman rank correlation coefficient 0.33 and 6×10^{-9} probability for a chance correlation, and

$$L = 1.70(\pm 0.76) \times 10^5 \times (\Sigma/{\rm g\,cm^{-2}})^{0.70\pm 0.18}\,L_\odot \tag{30}$$

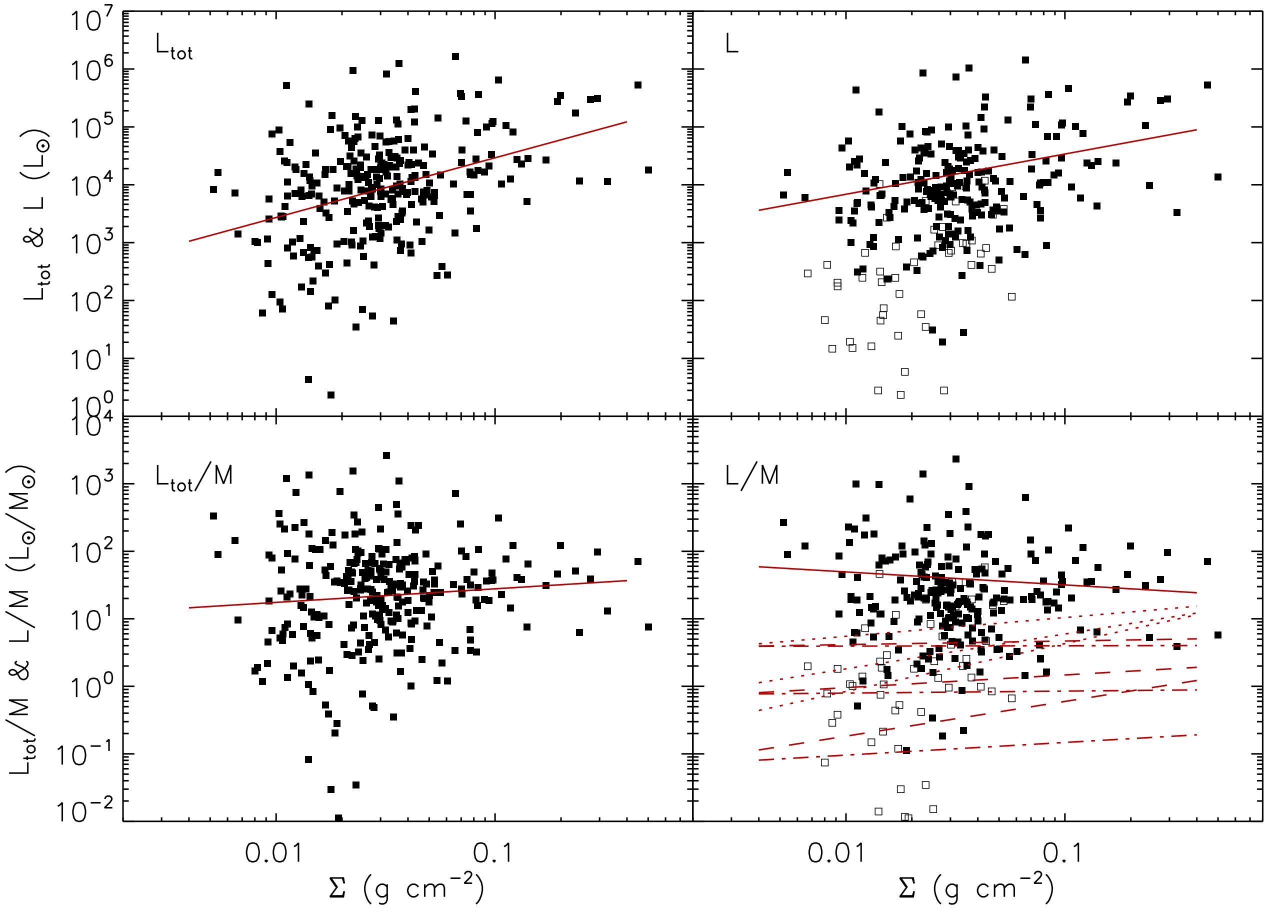

FIG. 8.— *(a) Top Left:* Correlation of $L_{\rm tot}$ with clump mass surface density Σ. Solid line shows the best-fit relation (see text). *(b) Top Right:* Correlation of L with Σ. Solid line shows the best-fit relation (see text). Open squares show clumps with uncertain measurements of F due to IRAS 100μm background subtraction (see Fig. 2b). *(c) Bottom Left:* Correlation of $L_{\rm tot}/M$ with Σ. Solid line shows the best-fit relation (see text). *(d) Bottom Right:* Correlation of L/M with Σ. Solid line shows the best-fit relation (see text). The three dashed lines show the minimum $L_{\rm min}/M$ expected from only ambient heating and accretion luminosity for clumps $M = 10^3\ M_\odot$, $T = 10, 15, 20$ K (from bottom to top) forming stars at fixed $\epsilon_{\rm ff} = 0.02$ (eq. 28). The three dash-dotted lines show the minimum $L_{\rm min}/M$ with mass $10^3 M_\odot$, $T = 10, 15, 20$ K (from bottom to top) forming stars at $\epsilon_{\rm ff} = 0.002$. The three dotted lines show the minimum $L_{\rm min}/M$ with mass $10^3 M_\odot$, $T = 10, 15, 20$ K (from bottom to top) forming stars at $\epsilon_{\rm ff} = 0.2$. Open squares show clumps with uncertain measurements of F due to IRAS 100μm background subtraction (see Fig. 2b).

with Spearman rank correlation coefficient 0.34 and 2×10^{-9} probability for a chance correlation.

In Fig. 8c and d, we plot the dependence of $L_{\rm tot}/M$ and L/M with Σ. We find best-fit relations:

$$L_{\rm tot}/M = 44.1(\pm 17.0) \times (\Sigma/{\rm g\,cm^{-2}})^{0.20\pm0.14}\ L_\odot/M_\odot \tag{31}$$

with Spearman rank correlation coefficient 0.07 and 0.26 probability for a chance correlation, and

$$L/M = 20.4(\pm 5.5) \times (\Sigma/{\rm g\,cm^{-2}})^{-0.19\pm0.14}\ L_\odot/M_\odot \tag{32}$$

with Spearman rank correlation coefficient -0.12 and 0.14 probability for a chance correlation.

One caveat of the above results is that L/M and Σ are inversely correlated via M, and this may be driving their apparent anti-correlation. Thus we also considered our other "good" cluster evolution indicators, F_w/F, $I_{\rm IRAC}$ and T_c and their dependence on Σ. However, we did not find any significant correlations of these properties with Σ.

In Fig. 8d we also show the predictions of eq. (28) for clumps with $M = 10^3\ M_\odot$, $T = 10, 15, 20$ K forming stars at fixed $\epsilon_{\rm ff} = 0.002, 0.02, 0.2$. Models with $T \sim 10 - 15$ K appear to define the lower boundary of the populated region of the observed L/M versus Σ parameter space, but obtaining precise constraints on $\epsilon_{\rm ff}$ is difficult because of the sensitivity of L/M to the adopted temperature. The models with high values of $\epsilon_{\rm ff} = 0.2$, even with $T = 10$ K appear to exceed the observed L/M of a significant number of the clumps, thus we tentatively conclude that $\epsilon_{\rm ff} < 0.2$. This analysis will be improved once FIR data become available allowing individual clump temperatures to be accurately measured from their spectral energy distributions. The implications of the detailed distribution of L/M of the clump population and its implication for star cluster formation theories will be examined in a future paper.

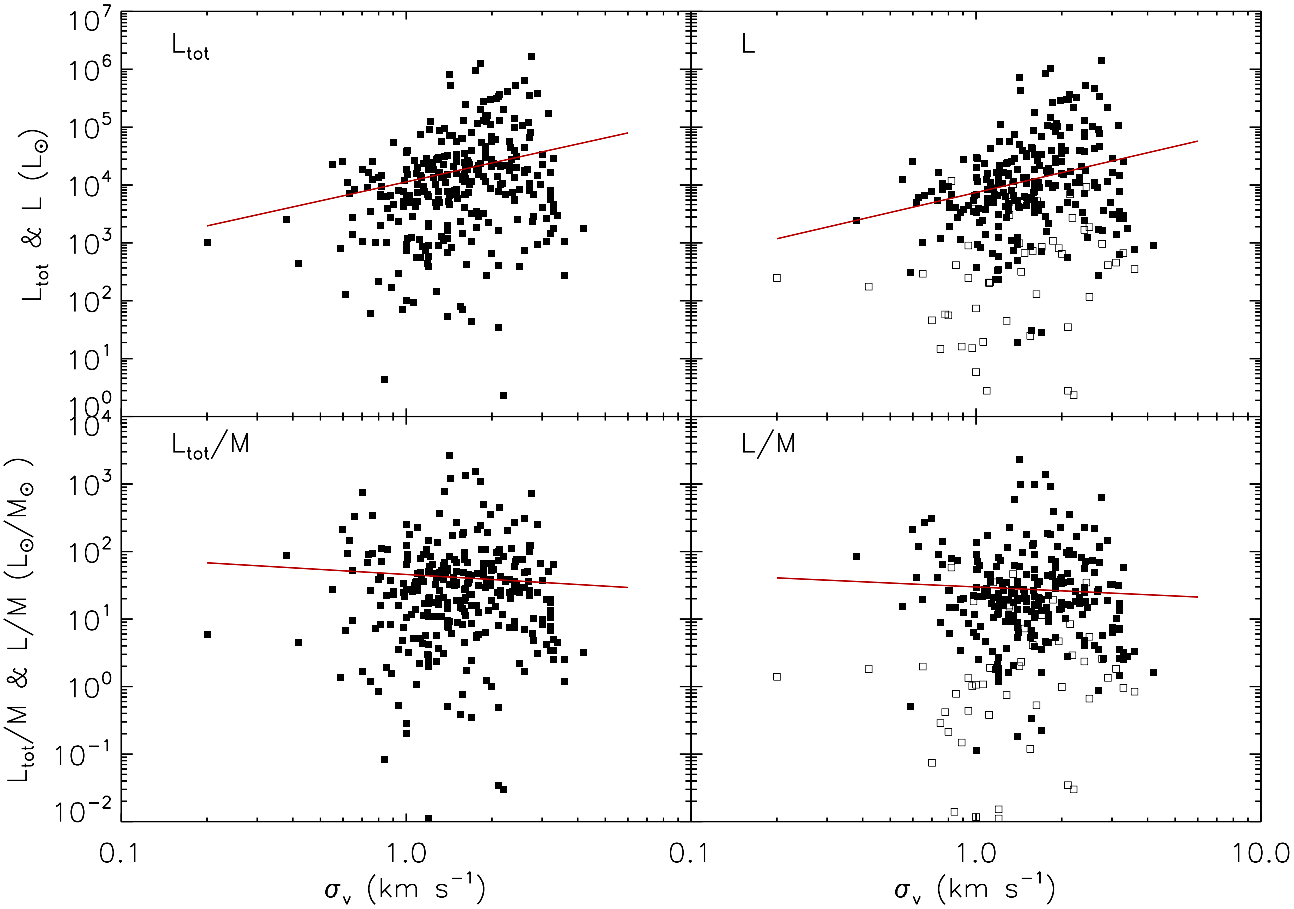

FIG. 9.— *(a) Top left:* Correlation of $L_{\rm tot}$ with σ_v. Solid line shows the best-fit relation (see text). *(b) Top right:* Correlation of L with σ_v. Solid line shows the best-fit relation (see text). *(c) Bottom left:* Correlation of $L_{\rm tot}/M$ with σ_v. Solid line shows the best-fit relation (see text). *(d) Bottom right:* Correlation of L/M with σ_v. Solid line shows the best-fit relation (see text). Open squares show clumps with uncertain measurements of F due to IRAS 100μm background subtraction (see Fig. 2b).

5.2. *Dependence of L and L/M with Velocity Dispersion and Virial Parameter*

In Fig. 9a and b, we explore the dependence of $L_{\rm tot}$ and L on the 1D velocity dispersion, σ, (as measured from HCO$^+$(1-0) in Paper I). We find best-fit relations:

$$L_{\rm tot} = 11300(\pm1900) \times (\sigma/{\rm km\,s^{-1}})^{1.09\pm0.26}\,L_\odot \tag{33}$$

with Spearman rank correlation coefficient 0.28 and 6.8×10^{-6} probability for a chance correlation, and

$$L = 7400(\pm1200) \times (\sigma/{\rm km\,s^{-1}})^{1.14\pm0.28}\,L_\odot \tag{34}$$

with Spearman rank correlation coefficient 0.26 and 3.2×10^{-5} probability for a chance correlation. We expect that σ correlates with M for clumps that are self-gravitating. Since L correlates with M, this can explain the observed, weaker correlation of L with σ.

Similarly, in Fig. 9c and d we show the dependence of $L_{\rm tot}/M$ and L/M with σ. We find best-fit relations:

$$L_{\rm tot}/M = 46(\pm6) \times (\sigma/{\rm km\,s^{-1}})^{-0.25\pm0.23}\,L_\odot/M_\odot \tag{35}$$

with Spearman rank correlation coefficient -0.05 and 0.41 probability for a chance correlation, and

$$L/M = 30(\pm4) \times (\sigma/{\rm km\,s^{-1}})^{-0.19\pm0.24}\,L_\odot/M_\odot \tag{36}$$

with Spearman rank correlation coefficient -0.04 and 0.46 probability for a chance correlation. Thus there is no apparent correlation of these variables. If star clusters were built-up hierarchically from a merger of smaller clumps, one might have expected to see increasing L/M with σ.

The virial parameter, $\alpha_{\rm vir} \equiv 5\sigma^2 R/(GM)$ (Bertoldi & McKee 1992), is proportional to the ratio of a clump's kinetic and gravitational energies. In Fig. 10a and b we show the dependence of $L_{\rm tot}$ and L with $\alpha_{\rm vir}$. We find best-fit

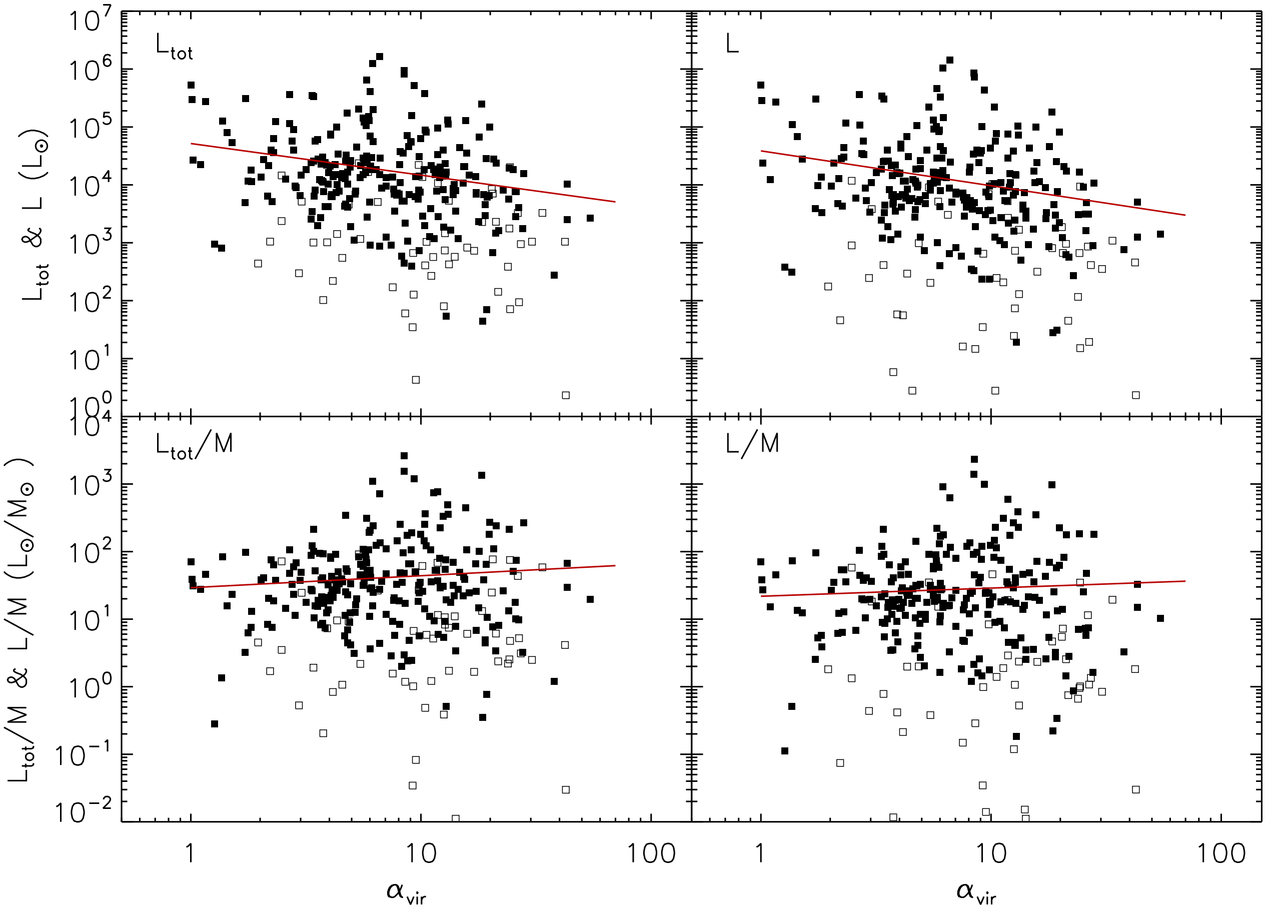

FIG. 10.— *(a) Top left:* Correlation of virial parameter α with $L_{\rm tot}$. Solid line shows the best-fit relation (see text). *(b) Top right:* Correlation of virial parameter α with L. Solid line shows the best-fit relation (see text). *(c) Bottom left:* Correlation of virial parameter α with $L_{\rm tot}/M$. Solid line shows the best-fit relation (see text). *(d) Bottom right:* Correlation of virial parameter α with L/M. Solid line shows the best-fit relation (see text). Open squares show clumps with uncertain measurements of F due to IRAS 100μm background subtraction (see Fig. 2b).

relations:

$$L_{\rm tot} = 52000(\pm 15000) \times (\alpha_{\rm vir})^{-0.55\pm0.14}\, L_\odot \tag{37}$$

with Spearman rank correlation coefficient -0.24 and 1×10^{-4} probability for a chance correlation, and

$$L = 39000(\pm 12000) \times (\alpha_{\rm vir})^{-0.60\pm0.15}\, L_\odot \tag{38}$$

with Spearman rank correlation coefficient -0.27 and 2×10^{-5} probability for a chance correlation. These (only moderately) significant correlations may be explained by the fact that smaller virial parameters indicate more gravitationally bound systems, which should be more prone to star formation. (Note that the absolute values of $\alpha_{\rm vir}$ are uncertain due to HCO$^+$ mass uncertainties, but relative values are better determined). However, these relations may alternatively be driven by the fact that more massive clumps tend to have smaller virial parameters (Paper I) and that luminosity correlates with mass (§4.4).

This second explanation appears to be supported by the following results. In Fig. 10c and d we show the dependence of $L_{\rm tot}/M$ and L/M with $\alpha_{\rm vir}$ (note, these are equivalent of correlating $L_{\rm tot}$ and L with $\sigma^2 R$). We find best-fit relations:

$$L_{\rm tot}/M = 29(\pm 8) \times (\alpha_{\rm vir})^{0.18\pm0.12}\, L_\odot/M_\odot \tag{39}$$

with Spearman rank correlation coefficient 0.06 and 0.36 probability for a chance correlation, and

$$L/M = 22(\pm 6) \times (\alpha_{\rm vir})^{0.12\pm0.13}\, L_\odot/M_\odot \tag{40}$$

with Spearman rank correlation coefficient 0.009 and 0.89 probability for a chance correlation. So these data do not reveal any correlation of cluster evolutionary stage (as measured by L/M) with degree of gravitational boundedness.

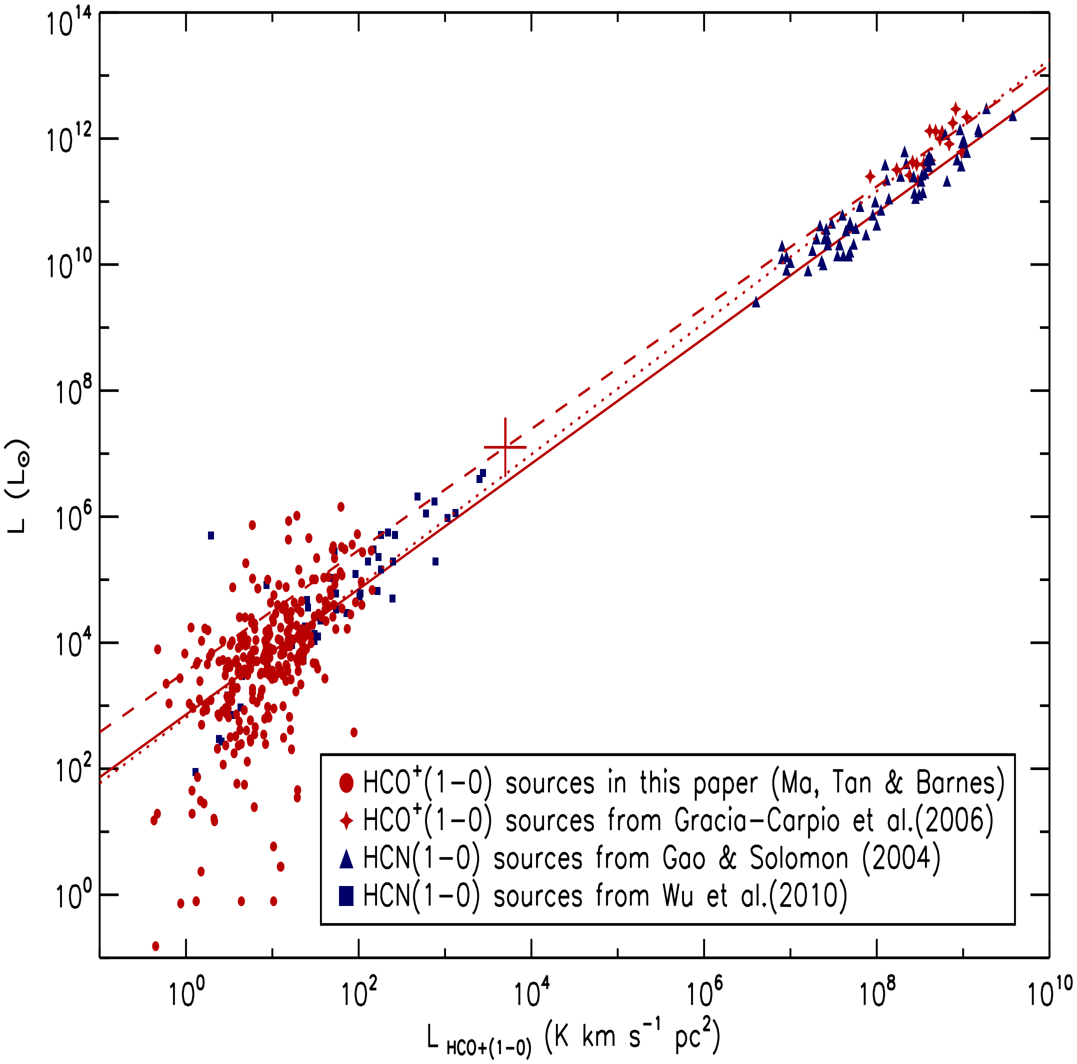

FIG. 11.— Bolometric luminosity, L, versus dense gas line luminosity, $L_{\mathrm{HCO^+(1-0)}}$. The CHaMP clumps are shown by filled red circles. The single large red cross shows the total luminosity and line luminosity of the whole CHaMP sample. Other HCO$^+$(1-0) data for entire galaxies from Graciá-Carpio et al. (2006) are shown by red stars. We also show HCN(1-0) data of galactic clumps (Wu et al. (2010) - blue squares) and entire galaxies (Gao & Solomon (2004) - blue triangles). The best fit relation to only the CHaMP HCO$^+$(1-0) data (filled red circles) is shown by a solid red line. The best fit relation to both the CHaMP (filled red circles) and extragalactic HCO$^+$(1-0) data (red stars) from Graciá-Carpio et al. (2006) is shown by a dotted red line. And the best fit relation to the total CHaMP data point (red cross) and the extragalactic sample (red stars) is shown by a dashed red line.

5.3. *Dependence of L with HCO$^+$(1-0) line luminosity*

Gao & Solomon (2004) found a tight linear correlation between the infrared luminosity (hereafter we refer to this as the bolometric luminosity, L) and the amount of dense gas as traced by the luminosity of HCN in both normal galaxies and starburst galaxies. This may suggest that the star formation rate (thought to be proportional to L, at least in starbursts) simply scales with the mass of dense gas. Similarly, Juneau et al. (2009) found an index of 0.99 ± 0.26 in their study of the relation between the bolometric luminosity and HCO$^+$ line luminosity in a sample of 34 nearby galaxies.

On the much smaller scales of clumps, the luminosity should not be such a good measure of SFR (Krumholz & Tan 2007), rather tracing embedded stellar content. Still, by surveying a sample of massive dense star formation clumps in CS(7-6), CS(2-1), HCN(1-0) and HCN(3-2), Wu et al. (2005, 2010) have extended the relation of $L - L_{\mathrm{HCN(1-0)}}$ proposed by Gao & Solomon (2004) down to $L \sim 10^{4.5} L_\odot$ (see Fig. 11).

The CHaMP survey provides a way to connect these scales, by being a complete census of dense gas and thus star formation activity over a several kpc^2 region of the Galaxy. The CHaMP clumps span the full range of evolution of these sources that will be averaged over in extragalactic observations. In addition, by its improved sensitivity, the CHaMP survey allows us to extend the bolometric luminosity versus dense gas line luminosity relation down to much smaller values of source bolometric luminosity.

In Fig. 11 we also plot the CHaMP sources. We fit a power-law relation between L and $L_{\mathrm{HCO^+(1-0)}}$ (because of the uncertainties in background subtracted luminosities, we only fit to those sources with $L > 10^{1.5} L_\odot$). Only fitting to the CHaMP clumps (via a least-squares fit in log L) yields:

$$\frac{L}{L_\odot} = 722(\pm 163)\left(\frac{L_{\mathrm{HCO^+(1-0)}}}{\mathrm{K\ km\ s^{-1}pc^2}}\right)^{1.00\pm 0.09} \tag{41}$$

Similarly, a fit to both the CHaMP sample and the extragalactic HCO$^+$(1-0) of Graciá-Carpio et al. (2006) yields:

$$\frac{L}{L_\odot} = 650(\pm 75)\left(\frac{L_{\mathrm{HCO^+(1-0)}}}{\mathrm{K\ km\ s^{-1}pc^2}}\right)^{1.04\pm 0.04} \tag{42}$$

Finally a fit to the total CHaMP data point and the extragalactic sample yields':

$$\frac{L}{L_\odot} = 3500(\pm 3000)\left(\frac{L_{\mathrm{HCO^+(1-0)}}}{\mathrm{K\ km\ s^{-1}pc^2}}\right)^{0.96\pm 0.05} \tag{43}$$

This last fit is expected to be the most accurate for extending current extragalactic results down to lower luminosities. Our results suggest that the $L - L_{\mathrm{HCO^+(1-0)}}$ relation in clumps (when averaged over a complete sample) is almost the same as that found when averaging over whole galaxies.

6. SUMMARY

A total of 303 dense gas clumps have been detected using the HCO$^+$(1−0) line in the CHaMP survey (Paper I). In this paper we have derived the SED for these clumps using Spitzer, MSX and IRAS data. By fitting a two temperature grey body model to the SED, we have derived the colder component temperature, colder component flux, warmer component temperature, warmer component flux, bolometric temperature and bolometric flux of these dense clumps. Adopting clump distances and HCO$^+$-derived masses from Paper I, we have calculated the bolometric luminosities and luminosity-to-mass ratios. These dense clumps typically have masses $\sim 700\ M_\odot$, luminosities $\sim 5 \times 10^4\ L_\odot$ and luminosity-to-mass ratios $\sim 70\ L_\odot/M_\odot$.

During the evolution of star-forming clumps, i.e. the formation of star clusters, the luminosity will increase and the gas mass will decrease due to incorporation into stars and dispersal by feedback, causing the luminosity-to-mass ratio to increase. So L/M should be a good evolutionary indicator of the star cluster formation process. The observed range of L/M from $\sim 0.1\ L_\odot/M_\odot$ to $\sim 1000\ L_\odot/M_\odot$ corresponds to that expected for evolution from starless clumps to those with near equal mass of stars and gas.

The fraction of the warmer component flux in the bolometric flux, F_w/F has a positive correlation with the luminosity-to-mass ratio, supporting the idea that as stars form in molecular clumps and L/M increases, a larger fraction of the bolometric flux will come out at shorter wavelengths. We also find that the colder component dust temperature, T_c, has a positive correlation with L/M: the bulk of the clump material appears to be getting warmer as star cluster formation proceeds. However, we caution that our measurements of T_c are relatively poor (they will be improved with the acquisition of *Herschel* observations in this region of the Galaxy). We also find a highly significant correlation of specific intensity in the *Spitzer*-IRAC bands (3-8 μm), I_{IRAC} with L/M. This has the potential to be a useful evolutionary indicator for the star cluster formation process.

We investigated the dependence of L/M with mass surface density, Σ, velocity dispersion, σ and virial parameter, α_{vir}. The lower limit of the distribution of L/M with Σ is consistent with a model for accretion luminosity powered by accretion rates that are a few percent of the global clump free-fall collapse rate. We do not see strong trends of L/M with Σ and, if present, real effects may be masked by the intrinsic correlation of these variables via M. Similarly, we do not find strong correlations between L/M and σ or α_{vir}.

The bolometric luminosity has a nearly linear correlation with the dense gas mass as traced by HCO$^+$(1−0) line luminosity, and this relation holds for over 10 orders of magnitude from molecular clumps in the Milky Way to infrared ultraluminous infrared galaxies. Our results have extended the previously observed relation of Wu et al. (2010) (via HCN(1−0) line observation) down to much lower luminosity clumps. The complete nature of our sample also gives a measurement at intermediate scales ($\sim$ several kpc^2) that connects the individual clump results with the extragalactic results, which are averages over clump populations.

JCT acknowledges support from NSF CAREER grant AST-0645412; NASA Astrophysics Theory and Fundamental Physics grant ATP09-0094; NASA Astrophysics Data Analysis Program ADAP10-0110.

Facilities: IRAS, MSX, Spitzer (IRAC), Mopra (MOPS)

APPENDIX

REFERENCES

Aumann, H. H., Fowler, J. W., & Melnyk, M. 1990, AJ, 99, 1674

Barnes, P. J., Yonekura, Y., Ryder, S. D., et al. 2010, MNRAS, 402, 73

Barnes, P. J., Yonekura, Y., Fukui, Y., et al. 2011, ApJS, 196, 12

Beltrán, M. T., Brand, J., Cesaroni, R., Fontani, F., Pezzuto, S., Testi, L., & Molinari, S. 2006, A&A, 447, 221

Bertoldi, F. & McKee, C. F. 1992, ApJ, 395, 140

Beuther, H., Schilke, P., Menten, K. M., Motte, F., Sridharan, T. K., & Wyrowski, F. 2002, ApJ, 566, 945

Bronfman, L., Nyman, L.-A., & May, J. 1996, A&AS, 115, 81

Egan, M. P., & Price, S. D. 1996, AJ, 112, 2862

Elmegreen, B. G. 2000, ApJ, 530, 277

Elmegreen, B. G. 2007, ApJ, 668, 1064

Faúndez, S., Bronfman, L., Garay, G., Chini, R., Nyman, L.-Å., & May, J. 2004, A&A, 426, 97

Foster, J. B., Jackson, J. M., Barnes, P. J., et al. 2011, ApJS, 197, 25

Gao, Y., & Solomon, P. M. 2004, ApJ, 606, 271

Graciá-Carpio, J., García-Burillo, S., Planesas, P., & Colina, L. 2006, ApJ, 640, L135

Gutermuth, R. A., Megeath, S. T., Myers, P. C., et al. 2009, ApJS, 184, 18

Hennebelle, P., & Falgarone, E. 2012, arXiv:1211.0637

Hildebrand, R. H. 1983, QJRAS, 24, 267

Hill, T., Burton, M. G., Minier, V., et al. 2005, MNRAS, 363, 405

Hunter, T. R., Churchwell, E., Watson, C., Cox, P., Benford, D. J., & Roelfsema, P. R. 2000, AJ, 119, 2711

Juneau, S., Narayanan, D. T., Moustakas, J., Shirley, Y. L., Bussmann, R. S., Kennicutt, R. C., & Vanden Bout, P. A. 2009, ApJ, 707, 1217

Kelly, B. C. 2007, ApJ, 665, 1489

Krumholz, M. R., & Tan, J. C. 2007, ApJ, 654, 304

Lada, C. J., & Lada, E. A. 2003, ARA&A, 41, 57

Ladd, E. F., Adams, F. C., Casey, S., Davidson, J. A., Fuller, G. A., Harper, D. A., Myers, P. C., & Padman, R. 1991, ApJ, 366, 203

Leitherer, C. et al. 1999, ApJS, 123, 3

Li, A., & Draine, B. T. 2001, ApJ, 554, 778

McKee, C. F., & Tan, J. C. 2003, ApJ, 585, 850

McKee, C. F., & Ostriker, E. C. 2007, ARA&A, 45, 565

Molinari, S., Brand, J., Cesaroni, R., & Palla, F. 2000, A&A, 355, 617

Molinari, S., Pezzuto, S., Cesaroni, R., Brand, J., Faustini, F., & Testi, L. 2008, A&A, 481, 345

Molinari, S. et al. 2010, A&A, 518, 100

Mueller, K. E., Shirley, Y. L., Evans, N. J., II, & Jacobson, H. R. 2002, ApJS, 143, 469

Myers, P. C., & Ladd, E. F. 1993, ApJ, 413, L47

Myers, P. C. et al. 1998, ApJ, 492, 703

Nakano, T., Hasegawa, T., Morino, J.-I., & Yamashita, T. 2000, ApJ, 534, 976

Ossenkopf, V., & Henning, T. 1994, A&A, 291, 943

Palla, F., & Stahler, S. W. 1992, ApJ, 392, 667

Preibisch, T., Ossenkopf, V., Yorke, H. W., & Henning, T. 1993, A&A, 279, 577

Sanders, D. B., & Mirabel, I. F. 1996, ARA&A, 34, 749

Schaller, G., Schaerer, D., Meynet, G., & Maeder, A. 1992, A&AS, 96, 269

Sridharan, T. K., Beuther, H., Schilke, P., Menten, K. M., & Wyrowski, F. 2002, ApJ, 566, 931

Stahler, S. W. 1988, ApJ, 332, 804

Tan, J. C. & McKee, C. F. 2002, in ASP Conf. Ser. 267, Hot Star Workshop III: The Earliest Phases of Massive Star Birth, ed. P. Crowther (San Francisco: ASP), 267

Tan, J. C., Krumholz, M. R., & McKee, C. F. 2006, ApJ, 641, L121

Tan, J. C., Shaske, S. N., & Van Loo, S. 2012, in *Molecular Gas, Dust, and Star Formation in Galaxies*, IAU Symp. 292, eds. T. Wong & J. Ott, (arXiv:1211.0198)

Whittet, D. C. B. 1992, Dust in the galactic environment Institute of Physics Publishing, 306 p.,

Wu, J., Evans, N. J., II, Gao, Y., Solomon, P. M., Shirley, Y. L., & Vanden Bout, P. A. 2005, ApJ, 635, L173

Wu, J., Evans, N. J., Shirley, Y. L., & Knez, C. 2010, ApJS, 188, 313

Yonekura, Y., Asayama, S., Kimura, K., et al. 2005, ApJ, 634, 476

TABLE 2

Parameters for the HCO^+(1-0) sources found in this survey.[a]

BYF No.	$\log(M)$ ($M_\odot$)	$T_{c,tot}$ (K)	$\log(L_{tot})$ ($L_\odot$)	$\log(L_{tot}/M)$ ($L_\odot/M_\odot$)	T_c (K)	$\log(L)$ ($L_\odot$)	$\log(L/M)$ ($L_\odot/M_\odot$)
5a	3.01	33.4	4.47	1.46	34.5	4.46	1.45
5b	2.13	30.5	3.43	1.29	29.5	3.15	1.01
5c	2.62	27.8	3.61	0.99	30.5	3.50	0.87
5d	2.95	34.9	4.65	1.70	36.3	4.64	1.69
7a	3.12	31.0	4.60	1.48	30.8	4.58	1.46
7b	2.71	34.7	4.28	1.57	35.6	4.27	1.56
9	2.65	21.5	3.03	0.38	23.0	2.85	0.20
11a	2.90	37.8	4.42	1.52	34.6	4.42	1.52
11b	2.68	32.4	3.46	0.77	31.0	3.34	0.66
11c	2.10	30.8	1.65	-0.45	24.9	1.45	-0.65
14*	1.99	24.2	2.64	0.65	26.5	2.24	0.26
15*	1.78	25.0	2.15	0.37	30.5	1.65	-0.13
16a	1.46	41.8	3.41	1.95	41.1	3.39	1.93
16b	2.30	25.8	2.95	0.64	22.2	2.82	0.51
16c*	2.04	25.2	2.75	0.71	29.2	2.32	0.28
16d	2.06	32.3	3.11	1.04	34.2	3.03	0.97
17a	2.11	31.0	3.34	1.23	36.0	3.28	1.17
17b	2.09	26.7	3.07	0.98	29.0	2.96	0.87
17c	2.55	25.7	3.05	0.50	27.2	2.86	0.31
19a*	2.13	27.4	2.92	0.78	36.7	2.50	0.37
19b	1.94	21.5	2.83	0.89	12.8	3.09	1.14
20*	2.39	24.5	2.63	0.24	29.2	2.11	-0.28
22	2.66	27.9	3.70	1.04	32.2	3.62	0.96
23a	2.65	30.4	3.88	1.24	29.0	3.83	1.19
23b	2.52	30.9	4.14	1.62	30.5	4.12	1.60
24	2.57	29.3	4.00	1.43	30.8	3.92	1.35
25a	3.06	29.7	4.39	1.33	34.0	4.34	1.28
25b	1.95	30.2	3.29	1.34	34.0	3.15	1.20
26	2.49	28.0	3.75	1.27	32.5	3.56	1.07
27*	2.17	26.7	3.15	0.98	30.7	2.47	0.30
32a	2.40	28.9	2.96	0.56	29.0	2.61	0.21
32b	2.12	26.9	2.87	0.75	31.9	2.37	0.25
36a	2.68	30.0	3.89	1.21	31.0	3.68	1.00
36b	2.81	33.6	4.14	1.33	31.4	4.07	1.25
36c	2.66	35.3	4.50	1.83	36.6	4.46	1.80
36d	2.65	29.9	3.93	1.28	30.2	3.79	1.14
36e	2.20	29.5	3.36	1.17	24.1	2.93	0.73
37a*	2.14	28.3	3.01	0.86	50.0	1.76	-0.38
37b*	1.84	29.3	2.87	1.03	41.4	1.87	0.03
38	2.10	35.0	3.30	1.20	35.3	3.28	1.18
40a	3.88	42.7	5.47	1.59	41.7	5.46	1.58
40b	3.70	34.1	4.90	1.20	34.3	4.83	1.13
40c	3.02	32.9	4.33	1.31	34.9	4.11	1.08
40d	3.38	34.5	5.06	1.68	33.9	5.03	1.65
40e	3.53	33.2	4.80	1.27	30.7	4.64	1.11
40f	3.59	31.9	4.78	1.19	30.4	4.60	1.01
40g	3.36	32.6	4.75	1.39	30.3	4.59	1.23
41	3.36	28.0	4.73	1.37	30.7	4.45	1.09
42a	2.74	28.7	4.07	1.33	29.3	3.81	1.07
42b	2.78	30.0	3.80	1.02	30.8	3.52	0.74
47*	2.83	26.6	3.37	0.54	28.8	2.95	0.12
54a	3.50	41.2	5.49	1.99	47.0	5.48	1.98
54b	3.78	39.5	5.44	1.66	40.7	5.43	1.65
54c	3.51	32.9	5.09	1.58	28.5	5.07	1.56
54d	3.54	42.6	5.56	2.02	43.7	5.56	2.02
54e	3.37	32.5	5.15	1.78	37.6	5.12	1.75

TABLE 2 — *Continued*

BYF No.	$\log(M)$ ($M_\odot$)	$T_{\rm c,tot}$ (K)	$\log(L_{\rm tot})$ ($L_\odot$)	$\log(L_{\rm tot}/M)$ ($L_\odot/M_\odot$)	$T_{\rm c}$ (K)	$\log(L)$ ($L_\odot$)	$\log(L/M)$ ($L_\odot/M_\odot$)
54f	3.25	32.7	4.34	1.09	36.1	4.21	0.97
54g	3.15	25.2	3.83	0.68	27.0	3.56	0.41
54h	3.17	32.1	4.14	0.97	34.3	3.86	0.69
56a	3.35	35.6	4.65	1.30	37.2	4.60	1.25
56b	3.02	26.3	3.55	0.53	24.4	3.42	0.40
56c*	2.84	22.8	3.25	0.40	21.5	2.82	-0.02
56d	2.97	29.2	3.66	0.69	28.7	3.48	0.51
57a	3.05	27.5	4.10	1.06	31.0	4.06	1.02
57b	2.54	21.2	3.27	0.73	16.9	3.20	0.65
60a	2.51	22.5	3.43	0.92	24.4	3.05	0.54
60b*	2.25	21.6	3.02	0.77	26.4	2.39	0.14
61a*	2.48	26.2	2.98	0.49	27.3	2.61	0.13
61b*	2.40	27.8	3.02	0.62	25.5	2.66	0.26
62	2.36	14.5	2.44	0.08	12.8	2.88	0.52
63*	2.24	26.1	2.59	0.34	28.0	2.07	-0.18
66	2.49	25.4	3.91	1.42	23.5	2.43	-0.06
67	2.63	24.0	3.17	0.53	22.8	2.79	0.16
68	3.43	24.4	4.35	0.92	29.6	4.22	0.79
69	2.55	30.3	4.13	1.58	30.3	3.98	1.43
70a	2.94	34.7	4.39	1.44	35.8	4.28	1.33
70b	3.05	35.3	4.32	1.27	37.6	4.21	1.16
71	2.63	30.5	3.88	1.25	31.1	3.49	0.86
72	3.38	27.5	4.22	0.84	31.7	3.99	0.61
73	3.16	31.3	4.44	1.28	34.8	4.41	1.25
76	2.76	24.5	3.78	1.03	21.4	3.89	1.13
77a	2.93	28.1	4.05	1.12	29.5	3.52	0.59
77b	3.27	33.2	4.07	0.80	31.5	3.99	0.72
77c	3.24	33.1	4.60	1.36	36.0	4.53	1.29
77d	2.68	34.5	4.18	1.50	33.5	4.03	1.35
78a	2.68	26.7	4.03	1.35	28.0	3.24	0.56
78b	3.01	26.7	3.90	0.89	28.5	3.55	0.55
78c*	2.62	23.2	3.02	0.40	23.8	2.55	-0.07
79a	2.82	31.4	3.47	0.65	29.6	3.26	0.44
79b	2.63	31.3	3.75	1.12	31.3	3.49	0.85
79c	2.74	29.6	3.25	0.51	29.3	2.95	0.21
83	2.74	32.6	4.18	1.44	32.0	3.94	1.20
85a	2.96	26.6	3.61	0.65	19.6	3.72	0.75
85b	3.01	30.1	3.84	0.83	28.5	3.42	0.41
85c	2.30	29.6	3.21	0.91	25.1	2.75	0.45
86a	2.78	30.5	3.75	0.97	34.1	3.39	0.61
86b	2.57	31.9	3.84	1.27	33.3	3.65	1.08
87	3.12	29.4	4.06	0.94	27.2	3.67	0.54
88	2.87	35.2	4.41	1.54	37.6	4.14	1.27
89a	2.45	30.2	3.45	1.01	26.0	3.21	0.76
89b	3.07	31.6	4.26	1.20	25.3	4.24	1.18
89c	2.14	30.4	3.30	1.15	27.0	3.10	0.95
90a	2.87	32.7	4.48	1.61	32.0	4.16	1.29
90b	2.78	33.8	4.33	1.55	32.9	4.04	1.26
90c	2.53	34.5	4.55	2.03	34.6	4.38	1.86
91a	3.24	31.2	4.75	1.51	35.0	4.54	1.30
91b	2.43	31.7	3.94	1.50	29.8	3.58	1.15
91c*	2.58	28.2	3.36	0.79	19.5	2.98	0.41
91d*	2.82	27.9	2.82	0.01	11.9	2.81	-0.01
91e	2.53	33.8	4.12	1.60	29.1	3.76	1.23
92a*	2.85	28.1	3.73	0.87	29.6	3.22	0.37
92b*	2.97	30.0	4.03	1.06	26.5	3.43	0.46
93a	3.13	34.6	4.85	1.72	37.8	4.66	1.53

TABLE 2 — *Continued*

BYF No.	log(M) ($M_\odot$)	$T_{\rm c,tot}$ (K)	log($L_{\rm tot}$) ($L_\odot$)	log($L_{\rm tot}/M$) ($L_\odot/M_\odot$)	$T_{\rm c}$ (K)	log(L) ($L_\odot$)	log(L/M) ($L_\odot/M_\odot$)
93b	2.82	35.5	4.82	2.00	38.5	4.66	1.84
93c	2.56	34.3	4.27	1.71	31.8	3.96	1.40
94a	2.98	34.3	4.48	1.50	33.2	4.25	1.26
94b	2.85	31.6	4.30	1.45	29.3	3.90	1.05
94c	2.79	33.6	4.25	1.46	32.9	4.04	1.25
94d	2.84	33.8	4.66	1.82	34.4	4.38	1.54
94e	2.19	35.1	4.02	1.83	33.5	3.70	1.51
94f	2.01	34.8	3.88	1.87	33.4	3.69	1.68
94g	2.40	34.6	4.44	2.04	34.9	4.31	1.92
94h	2.56	35.4	5.00	2.44	41.6	4.92	2.36
95a	2.94	35.2	4.10	1.16	32.7	3.77	0.83
95b	2.17	35.2	4.57	2.40	35.3	4.30	2.13
95c*	2.28	34.1	3.70	1.42	14.4	3.48	1.20
96	2.81	30.0	3.76	0.95	19.7	3.74	0.94
97	2.77	33.0	4.52	1.75	34.1	4.27	1.50
98a	2.93	39.6	5.20	2.28	44.7	5.00	2.08
98b*	2.53	39.6	3.93	1.39	46.1	3.27	0.74
98c*	1.89	45.1	0.37	-1.53	10.0	0.37	-1.52
99a	2.83	35.5	4.44	1.61	35.7	4.37	1.55
99b	2.75	35.5	4.56	1.80	39.3	4.48	1.73
99c	2.33	41.8	4.46	2.13	41.7	4.39	2.06
99d	1.88	38.2	4.41	2.54	32.2	4.03	2.15
99e	2.41	38.1	3.91	1.50	37.5	3.80	1.39
99f	1.99	42.9	4.38	2.38	50.0	4.24	2.25
99g	2.46	46.6	5.11	2.65	50.0	5.00	2.54
99h*	2.31	43.1	4.16	1.85	47.4	4.07	1.76
99i	2.10	43.5	4.98	2.88	45.2	4.88	2.78
99j	3.18	41.0	5.11	1.93	42.9	5.04	1.86
99k	2.91	40.1	5.30	2.38	47.0	5.16	2.25
99l	3.44	36.4	5.00	1.56	40.2	4.83	1.39
99m	3.52	39.4	5.53	2.00	50.0	5.48	1.96
99n	2.71	36.4	4.74	2.03	37.5	4.59	1.88
99o	2.46	33.4	4.15	1.69	32.0	3.88	1.42
99p	2.11	38.3	4.26	2.16	41.9	4.02	1.91
99q	2.51	36.8	4.02	1.51	38.8	3.79	1.29
99r	2.61	33.4	4.85	2.24	37.7	4.60	1.99
100a	3.04	34.2	4.76	1.72	34.8	4.41	1.37
100b	2.83	37.6	5.11	2.28	40.8	4.95	2.11
100c	1.96	39.7	4.29	2.33	37.1	4.22	2.27
100d*	2.53	34.8	4.22	1.70	32.2	3.71	1.18
100e*	2.43	36.0	4.27	1.83	38.7	3.72	1.28
100f	1.97	31.8	3.22	1.25	28.9	2.70	0.72
100g*	2.25	32.0	3.16	0.92	12.8	2.86	0.62
101a	2.17	35.6	3.89	1.72	34.0	3.73	1.55
101b	2.32	36.4	4.14	1.82	35.5	3.96	1.64
102a	2.24	38.7	3.82	1.58	38.1	3.53	1.29
102b	2.43	38.6	4.47	2.03	36.2	4.22	1.78
102c*	1.75	37.4	3.52	1.77	41.5	3.04	1.29
102d	1.56	40.0	3.81	2.26	41.1	3.35	1.79
103a*	2.41	38.8	4.37	1.96	48.2	3.96	1.54
103b*	2.43	39.5	4.30	1.88	42.5	3.97	1.54
103c	2.39	38.2	4.95	2.56	40.5	4.75	2.36
103d	2.48	39.0	4.17	1.69	37.7	4.04	1.56
103e	1.77	38.4	4.20	2.43	35.8	4.03	2.26
104a	1.40	42.1	4.27	2.87	32.8	3.89	2.50
104b	2.50	44.9	5.05	2.55	47.6	4.86	2.36
104c	2.43	43.5	5.12	2.69	46.7	5.02	2.59

TABLE 2 — *Continued*

BYF No.	$\log(M)$ $(M_\odot)$	$T_{\rm c,tot}$ (K)	$\log(L_{\rm tot})$ $(L_\odot)$	$\log(L_{\rm tot}/M)$ $(L_\odot/M_\odot)$	$T_{\rm c}$ (K)	$\log(L)$ $(L_\odot)$	$\log(L/M)$ $(L_\odot/M_\odot)$
105a	2.37	34.6	3.80	1.43	21.1	3.83	1.47
105b	3.16	35.9	5.18	2.02	40.3	4.92	1.76
105c*	2.64	29.2	2.86	0.22	35.6	-0.10	-2.74
105d*	2.92	35.2	4.34	1.43	26.0	3.84	0.92
105e	2.27	35.2	4.15	1.88	31.8	3.88	1.61
106a	2.47	36.0	4.13	1.66	34.2	3.91	1.44
106b	2.22	38.3	4.12	1.90	37.0	3.96	1.74
106c*	1.72	37.7	2.76	1.04	35.6	-0.10	-1.82
107a	2.22	37.4	4.18	1.96	36.2	4.07	1.85
107b	2.72	36.2	4.60	1.88	36.9	4.45	1.73
107c	2.54	34.8	4.80	2.26	36.5	4.64	2.10
107d	2.17	34.7	4.26	2.10	32.5	4.12	1.96
107e	2.73	36.9	4.39	1.66	36.3	4.05	1.32
107f	2.63	35.8	4.37	1.74	32.7	4.18	1.55
107g	2.52	36.4	4.33	1.81	31.7	4.02	1.50
107h*	2.35	33.3	4.14	1.79	23.2	4.01	1.66
107i*	1.88	36.3	3.51	1.64	25.8	2.93	1.06
108a	2.49	34.7	3.62	1.14	29.7	3.15	0.66
108b	2.93	34.0	4.75	1.82	36.3	4.54	1.62
108c*	2.24	35.1	3.36	1.12	35.3	2.91	0.67
108d*	1.96	33.8	3.85	1.89	26.5	2.82	0.86
109a	2.94	42.0	4.43	1.49	39.4	4.38	1.44
109b	2.35	34.4	3.87	1.52	35.6	3.77	1.42
109c	2.33	34.7	3.88	1.54	30.5	3.56	1.23
109d	1.99	33.4	3.83	1.84	27.3	3.65	1.66
109e	1.40	38.2	3.92	2.52	38.9	3.83	2.43
109f*	2.32	38.1	3.71	1.39	18.1	3.58	1.26
110a	2.93	35.1	4.86	1.93	39.4	4.70	1.77
110b	2.12	36.9	3.95	1.84	36.4	3.73	1.61
111a	3.53	33.1	5.08	1.56	39.0	4.97	1.44
111b	2.25	36.3	3.84	1.58	35.9	3.66	1.40
111c	1.92	33.8	3.40	1.47	31.9	3.10	1.18
111d	2.72	29.2	4.31	1.59	30.5	4.04	1.32
112*	2.69	31.0	3.66	0.97	26.9	2.99	0.30
113a	2.11	38.4	4.09	1.98	38.3	3.92	1.81
113b	1.96	39.5	4.31	2.35	38.7	4.20	2.24
114a	2.35	32.9	4.04	1.69	31.0	3.73	1.38
114b	2.30	37.5	3.82	1.52	31.7	3.61	1.31
114c	2.08	34.2	4.05	1.97	35.0	3.69	1.61
115a*	2.34	32.7	2.43	0.08	35.6	-0.10	-2.45
115b	1.94	35.7	3.98	2.04	35.7	3.84	1.90
115c	1.57	33.8	3.59	2.02	34.0	3.44	1.87
116a	2.12	33.6	3.54	1.42	32.7	3.08	0.95
116b	1.72	33.7	3.44	1.73	32.6	3.00	1.29
116c	2.10	34.3	3.79	1.70	34.7	3.48	1.38
117a	2.77	33.0	4.35	1.58	30.7	3.83	1.05
117b	2.46	34.8	3.87	1.41	32.7	3.52	1.07
117c*	1.85	30.6	-0.10	-1.95	35.6	-0.10	-1.95
117d	2.19	33.8	3.83	1.64	32.4	3.61	1.42
117e	2.45	34.3	4.12	1.67	32.7	3.88	1.42
118a	2.83	32.3	3.71	0.88	35.0	3.63	0.80
118b	2.39	33.4	3.95	1.56	31.2	3.71	1.32
118c	2.70	34.5	4.32	1.62	33.5	4.13	1.43
123a	2.47	25.2	2.77	0.30	23.2	2.54	0.08
123b*	2.75	26.1	2.47	-0.28	13.1	2.39	-0.36
123c*	2.70	23.8	2.01	-0.69	35.6	0.77	-1.93
123d*	2.42	22.6	2.34	-0.08	14.8	1.75	-0.67

TABLE 2 — *Continued*

BYF No.	$\log(M)$ ($M_\odot$)	$T_{\rm c,tot}$ (K)	$\log(L_{\rm tot})$ ($L_\odot$)	$\log(L_{\rm tot}/M)$ ($L_\odot/M_\odot$)	$T_{\rm c}$ (K)	$\log(L)$ ($L_\odot$)	$\log(L/M)$ ($L_\odot/M_\odot$)
126a	3.87	37.9	5.72	1.85	50.0	5.72	1.85
126b	2.82	37.2	4.91	2.09	43.1	4.88	2.06
126c	3.14	31.8	5.02	1.88	40.5	5.01	1.87
126d	2.64	39.9	4.46	1.81	44.1	4.40	1.76
126e	2.96	34.3	4.52	1.57	37.6	4.46	1.51
127*	1.28	20.7	2.10	0.83	35.6	-0.82	-2.09
128a	3.37	29.7	4.25	0.88	31.7	4.13	0.76
128b	3.46	34.5	5.54	2.09	50.0	5.53	2.08
128c	2.93	30.5	4.22	1.29	31.8	4.17	1.23
128d	2.83	37.4	4.53	1.70	37.7	4.49	1.66
128e	2.78	33.6	4.17	1.39	33.4	4.06	1.28
129a*	1.18	29.6	1.85	0.68	24.1	1.18	0.00
129b*	1.26	31.5	1.97	0.72	30.4	1.29	0.03
130a	2.18	24.9	2.65	0.47	28.6	2.52	0.33
130b	2.21	24.9	2.60	0.39	29.8	2.37	0.16
131a	3.53	39.5	5.24	1.71	37.0	5.02	1.49
131b	3.17	39.5	5.58	2.41	38.7	5.34	2.17
131c	3.32	41.4	5.81	2.49	43.3	5.66	2.34
131d	3.05	41.2	6.10	3.04	41.3	6.01	2.96
131e	2.79	42.7	5.98	3.19	43.9	5.93	3.14
131f	3.38	34.0	5.31	1.93	31.2	5.34	1.96
131g	3.18	31.1	4.95	1.77	31.9	4.75	1.57
131h	2.98	34.2	4.88	1.90	32.9	4.63	1.65
131i	2.45	33.5	4.18	1.72	29.8	3.73	1.28
132a	3.29	40.5	5.61	2.32	41.3	5.52	2.22
132b	2.64	35.7	5.72	3.08	42.4	5.64	3.00
132c	2.27	39.1	5.40	3.13	36.9	5.26	2.99
132d	3.36	39.8	6.22	2.86	40.6	6.16	2.80
132e	2.50	37.5	5.92	3.42	30.9	5.87	3.37
134a*	2.32	25.2	1.90	-0.41	20.6	1.39	-0.92
134b	2.03	22.7	1.73	-0.29	23.4	1.29	-0.74
134c	1.96	22.1	1.84	-0.11	22.1	1.49	-0.47
141a	2.03	29.5	3.09	1.07	31.0	2.92	0.89
141b	1.63	24.5	3.07	1.44	27.6	2.96	1.33
142a	2.04	35.8	3.72	1.68	35.9	3.70	1.66
142b	2.05	31.2	3.46	1.41	32.2	3.38	1.33
144a*	1.71	27.3	1.78	0.07	23.4	1.17	-0.54
144b*	2.04	27.7	2.23	0.19	25.2	1.21	-0.83
144c*	1.72	24.1	0.63	-1.08	35.6	-0.14	-1.85
149a	2.57	33.8	4.55	1.98	38.4	4.54	1.96
149b	1.70	31.0	3.86	2.16	31.9	3.78	2.08
150	2.45	29.9	3.80	1.36	31.3	3.61	1.17
161	2.37	34.4	3.89	1.52	34.2	3.73	1.36
162	2.66	33.5	4.00	1.34	33.1	3.86	1.20
163a	2.78	39.4	4.36	1.58	38.0	4.33	1.55
163b	2.65	39.2	4.01	1.36	36.2	3.96	1.31
163c	2.76	35.8	4.15	1.39	36.8	3.98	1.21
165a	2.53	35.1	3.84	1.31	34.6	3.74	1.21
165b	2.68	33.3	4.31	1.63	34.8	4.24	1.55
167a	2.26	30.3	3.67	1.41	29.3	3.58	1.31
167b	2.64	32.5	4.20	1.55	32.8	4.09	1.45
167c	2.17	31.1	3.72	1.54	30.6	3.58	1.41
183	2.78	23.6	2.91	0.13	31.2	2.49	-0.29
185	2.08	46.3	4.41	2.33	41.8	4.40	2.33
188*	2.72	23.2	3.00	0.28	17.3	2.62	-0.11
190a	2.75	27.1	3.62	0.87	27.8	3.55	0.80
190b	2.74	27.2	3.84	1.10	30.1	3.81	1.07

TABLE 2 — *Continued*

BYF No.	$\log(M)$ ($M_\odot$)	$T_{\rm c,tot}$ (K)	$\log(L_{\rm tot})$ ($L_\odot$)	$\log(L_{\rm tot}/M)$ ($L_\odot/M_\odot$)	$T_{\rm c}$ (K)	$\log(L)$ ($L_\odot$)	$\log(L/M)$ ($L_\odot/M_\odot$)
199a	2.89	26.3	3.81	0.92	29.6	3.68	0.79
199b	2.26	24.2	4.22	1.95	19.1	3.68	1.41
201a	2.71	29.9	3.91	1.20	28.7	3.65	0.94
201b	2.91	29.8	4.35	1.44	29.2	4.09	1.18
202a	3.52	24.0	2.98	-0.55	24.7	2.58	-0.95
202b*	2.79	24.8	3.02	0.23	44.4	1.66	-1.13
202c	3.02	31.6	4.27	1.25	31.6	4.22	1.20
202d	2.88	25.7	3.63	0.75	25.1	3.44	0.56
202e	2.67	25.9	3.28	0.62	27.3	3.10	0.43
202f*	2.71	25.3	2.74	0.03	35.6	0.45	-2.26
202g*	2.73	26.1	3.07	0.34	24.0	2.31	-0.42
202h*	3.00	23.3	1.54	-1.46	10.0	1.54	-1.46
202i*	2.92	23.0	2.61	-0.31	35.6	0.45	-2.48
203a	2.92	32.7	3.98	1.06	35.9	3.94	1.02
203b	2.79	25.1	3.55	0.76	24.8	3.46	0.67
203c	3.21	31.6	4.30	1.09	31.7	4.28	1.07
203d	2.90	34.5	4.21	1.31	35.3	4.20	1.29
208a	3.18	23.8	3.69	0.51	20.8	3.59	0.41
208b	2.51	23.3	2.96	0.45	23.8	2.77	0.26

[a] Here $\rm T_{c,tot}$ and $L_{\rm tot}$ are the colder component temperature and infrared luminosity using the non-background subtracted method. While $\rm T_c$ and L are derived using the background subtracted method.

[*] Clumps with uncertain measurements of L due to IRAS 100μm background subtraction (see Fig. 2b).